Density functional theory study of the structural and electronic properties of single and double acceptor dopants in MX_2 monolayers

Yuqiang Gao [1,2,*] and Paul J. Kelly [2,†]

[1] Department of Physics, School of Physics and Electronic Information, Anhui Normal University, Wuhu 241000, People's Republic of China
[2] Faculty of Science and Technology and MESA$^+$ Institute for Nanotechnology, University of Twente, P.O. Box 217, 7500 AE Enschede, Netherlands

(Received 21 September 2023; revised 9 November 2023; accepted 28 November 2023; published 20 December 2023)

Density functional theory calculations are used to systematically investigate the structural and electronic properties of MX_2 transition metal dichalcogenide monolayers with M = Cr, Mo, W and X = S, Se, Te that are doped with single (V, Nb, Ta) and double (Ti, Zr, Hf) acceptor dopants on the M site with local D_{3h} symmetry in the dilute limit. Three impurity levels that arise from intervalley scattering are found above the valence band maxima (VBM): an orbitally doubly degenerate e' level bound to the K/K' VBM and a singly degenerate a'_1 level bound to the Γ-point VBM. Replacing S with Se or Te lowers the Γ point VBM substantially with respect to the K/K' VBM bringing the a'_1 level down with it. The relative positions of the impurity levels that determine the different structural and electronic properties of the impurities in p-doped MX_2 monolayers can thus be tuned by replacing S with Se or Te. Single acceptors introduce a magnetic moment of 1 μ_B in all MX_2 monolayers. Out-of-plane magnetic anisotropy energies as large as 10 meV/dopant atom are found thereby satisfying an essential condition for long-range ferromagnetic ordering in two dimensions. For double acceptors in MS_2 monolayers, both holes occupy the high-lying a'_1 level with opposite spins so there is no magnetic moment; in MSe_2 and MTe_2 monolayers the holes occupy the e' level, a Jahn-Teller (JT) distortion wins the competition with exchange splitting resulting in the quenching of the magnetic moments. Even when the JT distortion is disallowed, magnetic double acceptors have a large in-plane magnetic anisotropy energy that is incompatible with long-range magnetic ordering in two dimensions. The magnetic moments of pairs of single acceptors exhibit long-range ferromagnetic coupling except for MS_2 where the coupling is quenched for impurity pairs below a critical separation. For Se and Te compounds, the holes are accommodated in high-lying degenerate e' levels, which form triplets for all separations. However, for X = Te, a JT distortion lifts the degeneracy of the e' levels leading to a reduction of the exchange interaction between impurity pairs. Deep, intrinsic, vacancy, and antisite defects that localize the holes might stabilize the magnetization of p-doped MX_2 monolayers. Our systematic study of the p-doped MX_2 monolayers identifies 1H $CrTe_2$ and $MoSe_2$ as the most promising candidates for room-temperature ferromagnetism. We combine the exchange interaction estimated from the energy difference calculated for ferromagnetically and antiferromagnetically coupled pairs with Monte Carlo calculations to estimate the Curie temperatures T_C for vanadium-doped $CrTe_2$ and $MoSe_2$ monolayers. Room-temperature values of T_C are predicted for V dopant concentrations of 5% and 9%, respectively. In view of the instability of $CrTe_2$ in the 1H form, we suggest that the $Cr_xMo_{1-x}(Te_ySe_{1-y})_2$ alloy system be studied. A single d electron or hole is uncorrelated. However, in the single-impurity limit, the residual self-interaction of this carrier in the local spin density approximation (LSDA) can be corrected by introducing a Hubbard U. Doing so leads to a large increase of the ordering temperatures calculated in the LSDA (reducing the doping concentration needed to achieve room-temperature ordering) but at the expense of introducing an indeterminate parameter U.

DOI: 10.1103/PhysRevB.108.245421

I. INTRODUCTION

The observation of ferromagnetism in Mn-doped InAs [1] and GaAs [2] semiconductors and predictions that room-temperature ordering might be attainable [3] stimulated attempts to realize such a dilute magnetic semiconductor (DMS). After twenty-five years and a very considerable research effort, the maximum ordering temperature has stagnated at values well below room temperature [4,5]. Research proceeds largely empirically with the number of semiconducting materials being considered multiplying without it becoming clear what the fundamental limits of the ordering temperatures are that can be achieved in a certain material system. There are many reasons for the low-ordering temperatures [6,7] but the main problem is that the open d shell states of magnetic impurities like Mn are quite localized. While this favors the on-site exchange interaction, which is the origin of the Hund's-rule spin alignment that makes the

*y.gao@ahnu.edu.cn
†Corresponding author: P.J.Kelly@utwente.nl

magnetic moment of the ion robust and insensitive to temperature, it leads to weaker exchange interactions between pairs of impurity ions that determine the Curie temperature T_C, the ferromagnetic ordering temperature. Attempts to increase T_C by increasing the concentration of dopant atoms are thwarted by their clustering or by the formation of antisite defects, which are electron donors that reduce the concentration of holes. Transition metal ions such as Mn, Fe, or Co induce "deep levels", tightly bound, partially occupied states in the fundamental gap of many semiconductors. At high dopant concentrations, these form deep impurity bands that dominate the (transport) properties of a material that, from the point of view of the electronic structure, is no longer a semiconductor but a completely new material.

Recently we explored a different approach to realizing a high-temperature magnetic semiconductor [8]. In a tight-binding picture, the transition metal (TM) d bandwidth is $2zt$ where z is the number of neighboring TM atoms and t is the nearest-neighbour hopping matrix element. Because of the low coordination number in two-dimensional materials, the TM dichalcogenide (TMD) MoS_2 with $z = 6$ has a substantially reduced d bandwidth W_d. This makes it easier to satisfy the Stoner criterion for the occurrence of itinerant ferromagnetism, $D(E_F)I_{xc} > 1$, where I_{xc} is the Stoner parameter and $D(E_F)$ is the density of states (DoS) at the Fermi level that is inversely proportional to the bandwidth. I_{xc} is essentially an atomic property and in the local spin density approximation (LSDA) [9,10] it contains contributions from both exchange and correlation [11–13].

Mo has a $4d^5 5s^1$ electronic configuration and in MoS_2 it is nominally Mo^{4+} with one up-spin and one down-spin d electron. A monolayer of MoS_2 is a direct gap semiconductor with a very narrow Mo d band containing these two electrons, the bold black band in Fig. 1(a), so it is nonmagnetic. This nonbonding band forms the top of the valence band in a gap formed by bonding and antibonding combinations of Mo-d and S-p states. To probe the enhanced DoS, we considered hole-doping MoS_2 by replacing some of the Mo atoms with group VB acceptor atoms [8].

When a group VIB Mo atom is replaced by a group VB atom like V, Nb, or Ta, then the dopant atom, e.g., V^{4+}, has a single unpaired d electron and therefore introduces a single hole into the narrow Mo 4d band; substitution of a group IVB atom (Ti, Zr, Hf) will introduce two holes per dopant atom. In the single-impurity limit, the asymptotic Coulomb potential of the ionized impurity leads to a series of hydrogenic states bound to the top of the valence band. At the $K(K')$ VBM, the highest such state is a doubly degenerate state with e' symmetry in the local D_{3h} symmetry that has mixed Mo $d_{x^2-y^2}$ and d_{xy} character. At the slightly lower Γ-point VBM the highest state is an a'_1 symmetry state with Mo $d_{3z^2-r^2}$ character and a large effective mass [14]. For finite concentrations of dopant atoms, these impurity states form impurity bands and at finite temperatures the holes in these impurity bands are thermally excited into the top of the narrow nonbonding Mo d band.

In Ref. [8] we found that pairs of V, Nb, and Ta substitutional dopants in an MoS_2 monolayer coupled ferromagnetically for all dopant separations but the shortest. In the single-impurity limit, a large out-of-plane magnetic anisotropy of ~5 meV per dopant ion was found that allows circumvention of the Mermin-Wagner theorem according to which thermal fluctuations destroy ordering in two dimensions for isotropic Heisenberg exchange [15,16]. Large single ion anisotropy (SIA) combined with isotropic exchange coupling leads to effective Ising spin behavior [17] and long-range magnetic ordering [18,19] at finite ordering temperatures that can be estimated using Monte Carlo calculations [20,21]. For V, Nb, and Ta, we estimated values of T_C of about 100 K for Nb and Ta and as high as 160 K for V for doping concentrations of order 9%. Very recent reports of long-range and/or room-temperature ferromagnetism occurring in V-doped WS_2 [22] and WSe_2 monolayers [23,24], in $MoSe_2$ and $MoTe_2$ [25], in V- and Ta-doped $MoTe_2$ [26,27] and in V-doped MoS_2 [28] (whereby the interaction with anion vacancies would appear to play an important role [28,29]) provide the motivation to investigate these systems more systematically.

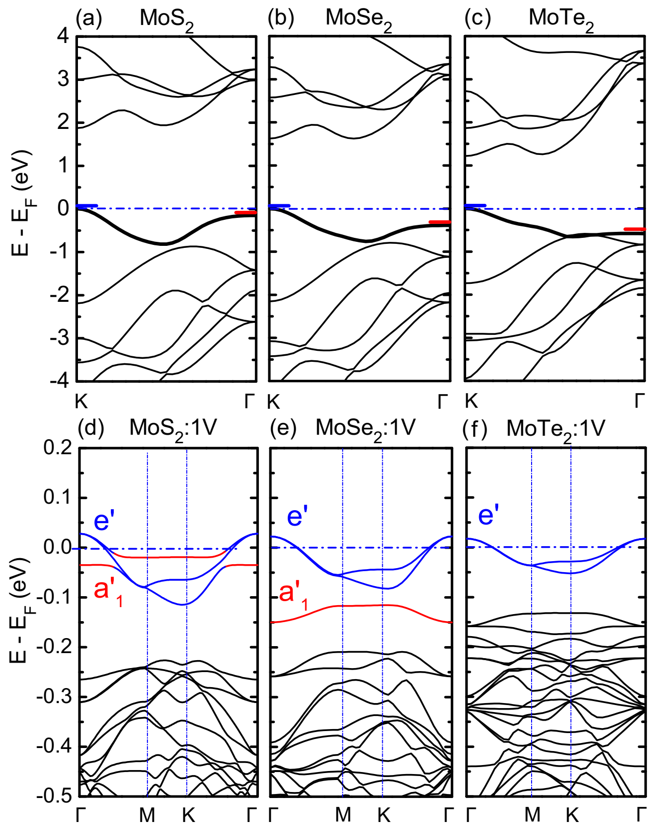

FIG. 1. Band structures without spin-orbit coupling of monolayers of undoped MoS_2 (a), $MoSe_2$ (b), and $MoTe_2$ (c) and with a single substitutional vanadium dopant atom on a Mo site in a 6×6 supercell [(d)–(f)]. The zero of energy is the Fermi level. In (a)–(c), the blue and red horizontal lines represent, respectively, the e' impurity levels bound to $\varepsilon(K/K')$, the K/K' valence band maxima (VBM), and the a'_1 impurity level bound to $\varepsilon(\Gamma)$, the Γ VBM. The energy difference $\varepsilon(K/K') - \varepsilon(\Gamma) = \Delta_{K\Gamma}$ increases in the sequence S → Se → Te. In (d)–(f) the blue and red lines are the corresponding bands formed from these impurity levels because of the finite size of the unit cell and the periodic boundary conditions. Note that different energy scales are used in the top and bottom panels.

In our study of MoS_2, we identified the formation of singlet states for dopant pairs closer than a critical separation (∼9 Å) as the most important factor limiting the ordering temperature to below room temperature in *p*-doped MoS_2 monolayers [8]. For close dopant pairs, the π interaction of a_1' states with $d_{3z^2-r^2}$ character is stronger than the σ interaction between e' states with $d_{x^2-y^2}$ and d_{xy} character so the highest-lying level occupied by the two holes is an antibonding a^* state. It is orbitally nondegenerate so to satisfy the exclusion principle the holes are forced to have opposite spins, i.e., the net magnetic moment is zero. Because of their $d_{3z^2-r^2}$ character, the a_1' states are very localized in the *xy* plane and the interaction between a_1' states decays more rapidly than that between e' states with $d_{x^2-y^2}$ and d_{xy} character. For separations larger than the critical distance, the orbitally degenerate antibonding e^* state can accommodate two holes with parallel spins corresponding to a ferromagnetic exchange interaction.

For $MoSe_2$ and $MoTe_2$, the Γ-point VBM is much lower than for MoS_2, compare Figs. 1(a)–1(c). We therefore expect that the a_1' levels will lie correspondingly low in energy and be fully occupied so quenching of the ferromagnetic interaction will not occur. However, there is a downside. Because of its spatial localization, the exchange splitting of the a_1' level is substantially larger than that of the e' levels making it much less sensitive to electronic thermal excitation. This will become important when the exchange splitting acquires the physical meaning of a stabilization energy for ferromagnetically coupled atoms. Because it is not *a priori* clear for which system the optimum interatomic exchange coupling and ordering temperature will occur, the purpose of this paper is to perform a systematic study of dopant acceptor levels in MX_2 monolayers with M = Cr, Mo, W; X = S, Se, Te in the single-impurity limit. We will also evaluate the magnetic anisotropy in this same limit because of the Mermin-Wagner theorem. Intrinsic defects such as vacancies and antisite defects are commonly observed in various van der Waals materials. The interplay between substitutional M dopants and intrinsic defects could have significant influence on the Curie temperature so we will also consider some representative examples of these.

The paper is organized as follows. After a brief summary of some computational details in Sec. II, the main results for the electronic and structural properties of *p*-doped MX_2 monolayers in the single-impurity limit are reported in Sec. III. The exchange interaction between single acceptor pairs and the consequences of these for room-temperature ferromagnetism are examined in Sec. IV. In Sec. V, we compare our results with those of other computational studies and consider experiments in the light of our results. Section VI contains a brief summary and some conclusions.

II. COMPUTATIONAL METHOD

First-principles density functional theory (DFT) calculations were performed with a plane-wave basis and the projector augmented wave (PAW) formalism [30] as implemented in the VASP code [31–33]. An energy cut-off of 400 eV was used and atomic structures were fully relaxed until all forces were smaller than 0.01 eV/Å. Monolayers of MX_2 were periodically repeated in the *c* direction with a separation of more than 20 Å of vacuum to avoid spurious interactions that arise from the use of (artificial) periodic boundary conditions. Because we only consider free-standing monolayers, there was no need to take van der Waals interactions into account. The local (spin) density approximation, L(S)DA, underestimates equilibrium atomic separations more than generalized gradient approximations (GGA) overestimate them. However, by comparison with experiment, the LDA describes the relative positions of the valence band maxima better than does the GGA [8]. Since this will play an important role in our study of shallow impurity levels, we used the LSDA as parameterized by Perdew and Zunger [34]. A 12×12 supercell was used to reduce to an acceptable degree the interaction between impurities in neighboring supercells when modeling dopants in the single-impurity limit. A 2×2 k-point sampling was used for structure relaxation and 4×4 for the calculations with spin-polarization and spin-orbit coupling; a lower k-point sampling does not describe the magnetism sufficiently well. For intrinsic defects, a smaller 6×6 supercell was found to be sufficient to describe the defect potential inside the supercell reliably because of the greater localization of the gap states. For structural relaxation, we used Gaussian smearing and a broadening of 0.01 eV [35]. For more accurate total energies, the linear analytical tetrahedron method [36] with nonlinear corrections [37] was used.

III. RESULTS: SINGLE-IMPURITY LIMIT

We begin this section with a brief comparison of the calculated structural and electronic properties of pristine MX_2 monolayers in Sec. III A. In Sec. III B, we examine the structural and electronic properties of single and double acceptors in MX_2 monolayers. A number of intrinsic defects is considered in Sec. III C before briefly looking at the case of electron doping by the 5*d* element rhenium in Sec. III D.

A. MX_2 monolayers

Under ambient conditions, MoX_2 and WX_2 with X = S, Se, Te have a so-called "H" structure in which a hexagonal plane of M atoms is sandwiched between layers of X atom such that each M atom sits at the center of a trigonal prism with local D_{3h} symmetry, Fig. 2. Bulk structures are composed of van der Waals bound stacks of such layers in the *z* direction perpendicular to the basal planes with one (1H) or two (2H) layers in the periodic unit cell [49]. $CrSe_2$ is reported to be have been prepared in a metastable "T" structure [50] where one of the X-atom planes is rotated about the *z* axis by 180° so that each Cr atom sits at the center of a regular octahedron of X atoms. 1T CrS_2 and $CrSe_2$ are claimed to be metastable [51] and a mixed 1H, 1T, and 1T′ phase of CrS_2 was reported to be formed by chemical vapor decomposition [52]. To realize a ferromagnetic semiconductor, we will focus on doping the semiconducting 1H phase MX_2 monolayers and will include CrX_2 for the purposes of comparison. Experimentally, a monolayer of WTe_2 is found to be semimetallic with a T_d polytype structure [53] and will not be considered further in this paper.

The equilibrium structural and electronic parameters for 1H-MX_2 monolayers as calculated in the LDA [34] are listed

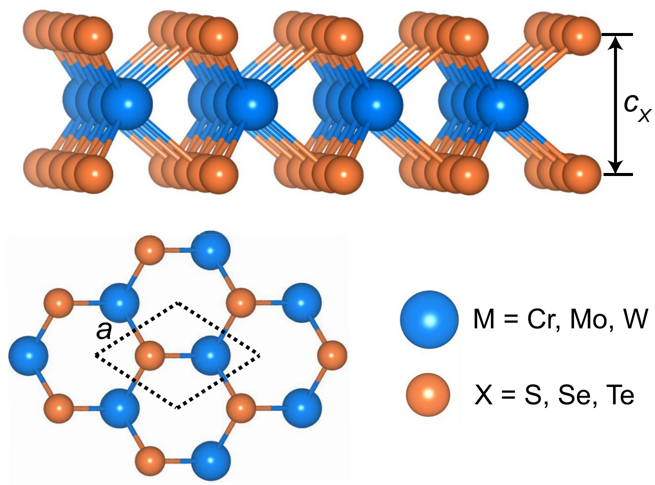

FIG. 2. Side view and top view of the atomic structure of an MX_2 ($M =$ Cr, Mo, W; $X =$ S, Se, Te) monolayer. The unit cell is enclosed by the dotted lines.

in Table I and, where possible, compared to experiment. The lattice constant a is seen to increase as X goes from S $\rightarrow$ Se $\rightarrow$ Te. This leads to a reduction in the overlap of M d orbitals and consequently of the bandwidth W of the "nonbonding" d band that forms the topmost valence band in Figs. 1(a)–1(c). The direct bandgap $\Delta\varepsilon_g$ at the K point decreases from MS_2 to MTe_2, while the energy difference $\Delta_{K\Gamma} = \varepsilon_\upsilon(K) - \varepsilon_\upsilon(\Gamma)$ between the K/K' and Γ VBM increases in the same sequence both with and without SOC. The experimental $\Delta_{K\Gamma}$ listed in Table I are obtained from ARPES measurements and include SOC.

Even though the lattice constant increases in the sequence $CrX_2 \rightarrow MoX_2 \rightarrow WX_2$, as M is changed from Cr to W the bandwidth W increases. The overlap of the M d orbitals that determines W is related not only to the M-M bond length but is also determined by the spatial extent of the outermost d orbitals. As we progress from $3d \rightarrow 4d \rightarrow 5d$, the outermost d orbitals must be orthogonal to the more strongly bound lower-lying ones, are therefore excluded from the region of space closest to the nucleus and end up having a larger spatial extent. The bandgap $\Delta\varepsilon_g$ also increases with increasing atomic number of M because the greater spatial extent of the d orbitals leads to a stronger bonding-antibonding interaction with the X, p orbitals pushing the uppermost four empty d states higher in energy. $\Delta_{K\Gamma}$ exhibits a similar trend except for the CrS_2 monolayer. In the next section, we will see that the properties of dopants are largely determined by those of the host material suggesting directions to explore to increase the ferromagnetic ordering temperatures.

B. Structural and electronic properties of *p*-doped MX_2 monolayers in the single impurity limit

We begin this section by calculating the formation energy of single and double acceptors in MX_2 monolayers, Sec. III B 1. The impurity binding energies calculated relative to the VBM are presented in Sec. III B 2 while the magnetic moments and exchange splittings calculated for each dopant are presented in Sec. III B 3. Before considering JT distortions for single and double acceptors in Secs. III B 5 and III B 6, we briefly consider the effect of symmetry-preserving relaxation in Sec. III B 4. Single ion anisotropy energies are presented in Sec. III B 7.

1. Formation energy

The formation energy of an M' dopant atom on an M atom host site, defined as

$$E_{\text{form}}[M'_M] = E_{\text{tot}}[MX_2\!:\!M'] - E_{\text{tot}}[MX_2] + \mu_M - \mu_{M'} \quad (1)$$

determines how easily doping is achieved. $E_{\text{tot}}[MX_2\!:\!M']$ is the total energy of a relaxed supercell of an MX_2 monolayer with a single M atom replaced with an M' dopant atom. $E_{\text{tot}}[MX_2]$ is the total energy of the same size supercell but for a pristine MX_2 monolayer. μ_M and $\mu_{M'}$ are the chemical potentials of M and M' atoms in their bulk bcc, respectively bcc or hexagonal, metallic phases. A negative formation energy in Table II indicates that substitutional doping of a group IVB or VB element in a monolayer of MX_2 is energetically favorable. The positive formation energies for some V-doped MX_2 monolayers are quite small relative to the magnitude of the heat of formation of MX_2 indicating that V doping is experimentally feasible. Globally, the formation energy increases in size from V to Ta, reaches a maximum size for Ti and is smaller for Zr and Hf. The formation energies of double acceptors are larger than those of single acceptors.

TABLE I. Structural and electronic properties of 1H-MX_2 monolayers. Shown are the lattice constant a and the separation of the two chalcogen X layers c_X, both in Å; the direct bandgap at the K point $\Delta\varepsilon_g$, the energy difference $\Delta_{K\Gamma} = \varepsilon_\upsilon(K) - \varepsilon_\upsilon(\Gamma)$ between the VBM at K and Γ without (with) spin-orbit coupling and the bandwidth W of the "nonbonding" band forming the top of the valence band, all in eV.

	X	S					Se					Te				
	M	a	c_X	$\Delta\varepsilon_g$	$\Delta_{K\Gamma}$	W	a	c_X	$\Delta\varepsilon_g$	$\Delta_{K\Gamma}$	W	a	c_X	$\Delta\varepsilon_g$	$\Delta_{K\Gamma}$	W
	Cr	2.97	2.92	1.07	0.22 (0.25)	0.95	3.12	3.11	0.87	0.32 (0.36)	0.86	3.37	3.38	0.62	0.45 (0.49)	0.70
Calc	Mo	3.12	3.11	1.87	0.15 (0.22)	1.06	3.25	3.31	1.62	0.38 (0.44)	1.02	3.47	3.59	1.22	0.58 (0.66)	0.86
	W	3.12	3.12	2.01	0.17 (0.35)	1.30	3.25	3.31	1.72	0.43 (0.55)	1.22					
	Cr															
Expt	Mo	3.16[a]	3.17[a]	1.90[b]	0.14[c]		3.29[a]	3.34[a]	1.58[d]	0.44[e]	0.90[e]	3.52[f]	3.60[f]	1.10[g]		
	W	3.15[h]	3.14[h]	2.01[i]	0.24[j]		3.28[h]	3.34[h]	1.66[k]	0.50[e]	1.24[e]					

[a]Reference [38]; [b]Reference [39]; [c]Reference [40]; [d]Reference [41]; [e]Reference [42]; [f]Reference [43]; [g]Reference [44]; [h]Reference [45]; [i]Reference [46]; [j]Reference [47]; [k]Reference [48].

TABLE II. Calculated formation energies in eV of various substitutional dopants M' on M sites (M'_M) in MX_2 monolayers with relaxation.

M	S			Se			Te	
M' X	Cr	Mo	W	Cr	Mo	W	Cr	Mo
V	−0.26	0.25	0.24	−0.37	0.32	−0.07	−0.45	0.22
Nb	−0.25	−0.15	−0.10	−0.55	−0.14	−0.49	−0.62	0.03
Ta	−0.36	−0.23	−0.02	−0.43	−0.10	−0.39	−0.57	0.07
Ti	−0.32	−0.58	−0.64	−0.74	−0.57	−0.72	−0.62	−0.33
Zr	−0.25	−0.25	−0.21	−0.46	−0.27	−0.55	−0.56	−0.21
Hf	−0.42	−0.32	−0.39	−0.52	−0.31	−0.84	−0.59	−0.42

Substituting chalcogen X atoms with M atoms or TM impurities in MX_2 would create antisite defects M_X as well as TM_X. As indicated in [54] and in Sec. III C, this will be energetically unfavorable compared to the substitution of M atoms. According to [55], TM impurities occupying the chalcogen site, TM_X, can be energetically favorable in postsynthesis impurity introduction. However, in the present paper, we focus on substituting M atoms with shallow impurities M' by impurity codeposition whereby holes can be introduced into the valence band maximum of MX_2 instead of into trapped (deep) impurity levels.

2. Binding energy

In effective mass theory (EMT), attractive and repulsive Coulomb potentials lead to the formation of Rydberg series of (shallow impurity) levels ε_n with $n = 1, 2, 3 \ldots$ bound to the conduction band minima and valence band maxima, respectively [56–58]. On substituting an M atom (M = Cr, Mo, W) in an MX_2 monolayer with a single (V, Nb, Ta) or a double (Ti, Zr, Hf) acceptor in the single-impurity limit, the repulsive impurity potential and intervalley scattering leads to the formation of an orbitally twofold degenerate e' level and a singly degenerate a'_1 level bound to the K/K' and Γ VBM, respectively [8]. The higher ($n \geqslant 2$) impurity levels are too shallow to show up above the VBM in the 12×12 supercell size we standardly use [8] and therefore only the e' and a'_1 impurity levels will be considered here. The impurity binding energy, defined as the position of the level with respect to the VBM, determines the degree of localization of the impurity wavefunction.

To establish the position of impurity levels with respect to the VBM, we first need to be able to identify the VBM in a doped system, something which is not trivial in a supercell calculation because of the interaction of Coulomb bound states with their periodic images and the overlapping of the resulting impurity bands with the VBM [8]. First, because the binding energies of both single and double acceptors in MX_2 monolayers, shown in Fig. 3, are much smaller than the sizable bandgaps seen in Table I, there is no overlap between the impurity bands and the conduction band minima (CBM). Second, because a repulsive Coulomb potential does not affect the conduction band states, in particular the states forming the CBM, we can determine the bulk VBM in a doped system from its position relative to the CBM in the pristine case ($\varepsilon_{\rm VBM} = \varepsilon_{\rm CBM} - \Delta\varepsilon_g$). Alternatively, we can align the VBM to a core level of an atom far from the dopant site, e.g., the Mo 4s level, extrapolating to infinite separation and relating that to the corresponding energy separation of the core level and VBM in a pristine MX_2 monolayer. The two procedures yield consistent results [8]. Because of its greater convenience, we use the first procedure to extract the position of the VBM here. The position of single (V, Nb, Ta) and double (Ti, Zr, Hf) acceptor impurity levels with respect to the VBM in doped MX_2 monolayers determined in this way are shown in Fig. 3. Because of the finite dispersion of the impurity bands in a supercell calculation, what is shown is the appropriate weighted average over the Brillouin zone of the impurity band.

For monolayers of MoS_2 [8], the a'_1 and e' levels are almost degenerate and the binding energy of single acceptor levels decreases from V to Ta as shown on the left-hand side of Fig. 3 (lhs, middle). The energy difference $\Delta_{K\Gamma}$ between the K/K' and Γ VBM in defect-free MX_2 monolayers determines the relative position of the impurity levels bound to these VBM. As shown in Fig. 1 and tabulated in Table I, $\Delta_{K\Gamma}$ increases as X goes from S to Te, so the a'_1 levels (red lines) will drop fast with respect to the e' levels (blue lines) going from MoS_2 to $MoTe_2$, which makes the a'_1 levels in $MoSe_2$ and $MoTe_2$ merge with the VBM in the 12×12 supercell we use, Fig. 3. The e' levels drop slightly from MoS_2 to $MoTe_2$. In $MoTe_2$, a Jahn-Teller distortion splits the degenerate e' levels; we return to this in Sec. III B 5.

In single-acceptor-doped CrX_2 monolayers (top left), the impurity binding energies exhibit trends similar to those found in MoX_2. However, the binding energies are lower and for CrS_2 the e' level is bound more strongly than the a'_1 level so the hole occupies the former. In WX_2 (bottom left) the impurity binding energies are almost the same as in MoX_2.

For the double acceptor levels shown on the right-hand side (rhs) of Fig. 3, the main trends for the a'_1 and e' levels in MX_2 parallel those found for single acceptors. The main difference is that the impurity binding energies of double acceptors are larger than those of single acceptors; the stronger repulsive potentials of the M'^{2-} ions (attractive for holes) affect the localized out-of-plane a'_1 levels more than the in-plane e' states. The a'_1 levels with $d_{3z^2-r^2}$ character lie well above the e' levels and accommodate both holes in Ti-, Zr-, and Hf-doped MS_2. In MSe_2, and MTe_2 they follow the Γ-point VBM down in energy, losing their holes to the orbitally degenerate e' levels that, being partly filled, are susceptible to Jahn-Teller distortion. The competition between Jahn-Teller distortion and spin polarization will be discussed in Sec. III B 6 for double-acceptor-doped MSe_2 and MTe_2.

3. Spin polarization

The results of calculating the magnetic moments of MX_2 monolayers with different dopants in 12×12 supercells including full structural relaxation are given in Table III. In the single-impurity limit, the magnetic moments are expected to be an integer number of Bohr magnetons μ_B. For all three single acceptors V, Nb, and Ta in MoS_2, this is true and the polarization is complete. The same is true for $MoSe_2$ and $MoTe_2$, Fig. 3 (lhs, middle).

CrX_2 monolayers doped with single acceptors also have a magnetic moment of $1\mu_B$ for all three single acceptors,

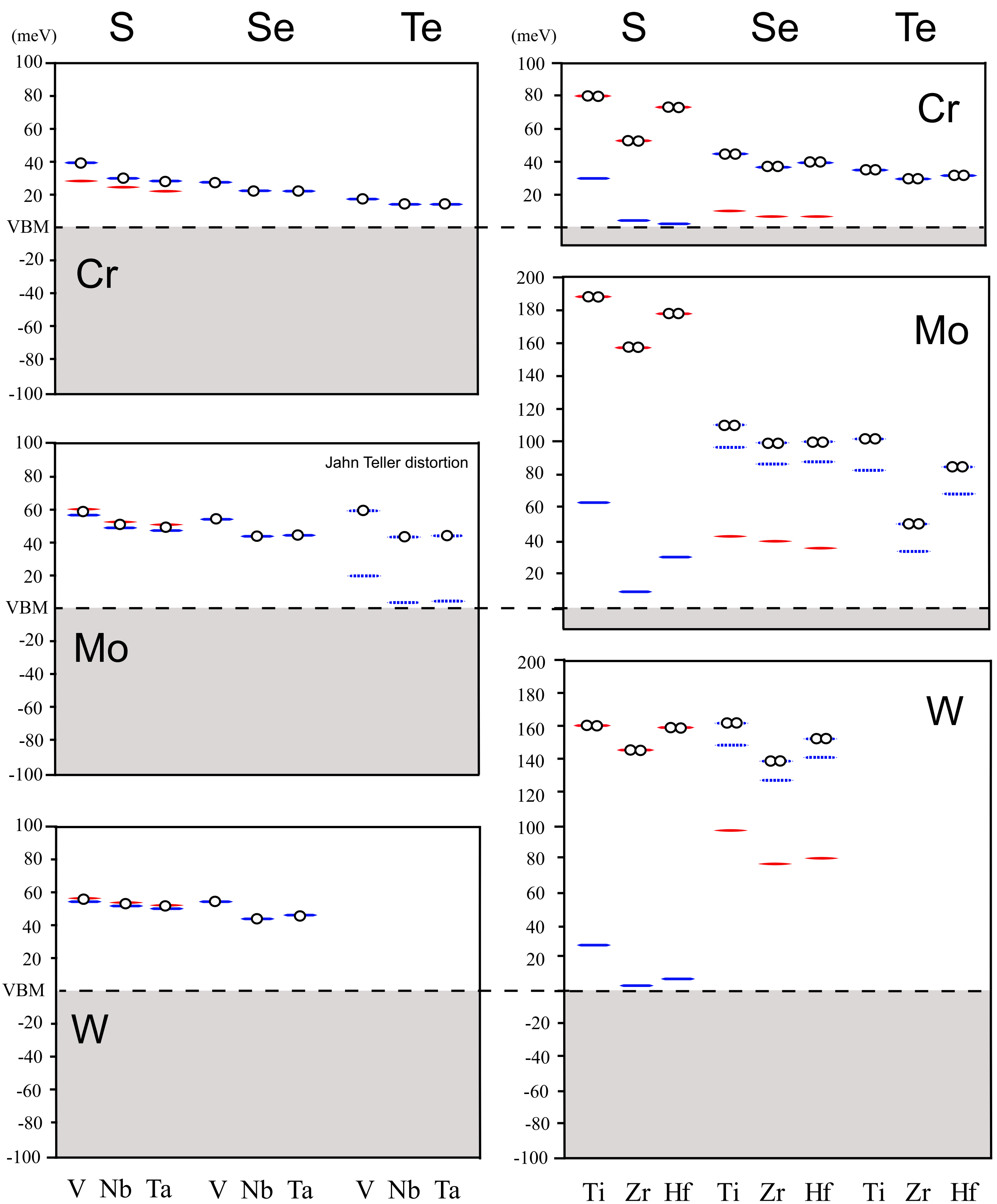

FIG. 3. Impurity levels for single (V, Nb, Ta) and double (Ti, Zr, Hf) acceptors in MX_2 monolayers including atomic relaxation but without spin polarization. All energies are shown in meV with respect to the top of the valence band. The short horizontal red and blue lines represent a_1' and degenerate e' levels, respectively. The dotted blue lines indicate the Jahn-Teller split e' levels. Holes represented by open circles occupy the highest levels in each system. Note that the smallest bandgap is large on the energy scale of the figure.

TABLE III. Calculated magnetic moments in μ_B for monolayers of MX_2 (12×12 supercell) doped with various transition metal atoms M' substituting a single M. The structures are fully relaxed with spin polarization. Jahn-Teller distortion is included for single but not for double acceptors; the competition between spin-polarization and Jahn-Teller splitting will be found to quench the magnetic moments in double-acceptor-doped $MoSe_2$, WSe_2, and $MoTe_2$ monolayers (*italics*).

X		S			Se			Te	
M'	M	Cr	Mo	W	Cr	Mo	W	Cr	Mo
V		1.00	1.00	1.00	1.00	1.00	1.00	1.00	1.00
Nb		1.00	1.00	0.91	1.00	1.00	0.71	1.00	1.00
Ta		1.00	1.00	0.90	1.00	1.00	0.70	1.00	1.00
Ti		0.00	0.00	0.00	2.00	(*2.00*)	(*2.00*)	2.00	(*2.00*)
Zr		0.00	0.00	0.00	2.00	(*2.00*)	(*2.00*)	2.00	(*2.00*)
Hf		0.00	0.00	0.00	2.00	(*2.00*)	(*2.00*)	2.00	(*2.00*)

(lhs, top). Even though the defect levels of Nb and Ta acceptors in WX_2 (lhs, bottom) are as deep as in MoX_2 and deeper than in CrX_2, see Fig. 3 (lhs), their magnetic moments are less than 1μ_B. This incomplete polarization can be attributed to the use of a finite, 12×12 supercell. If a supercell is not sufficiently large, then the interaction between dopants in neighboring cells leads to the formation of bands by the discrete impurity levels. Unless the exchange splitting is larger than the impurity bandwidth, this will result in noninteger values of $n_\uparrow$ and $n_\downarrow$ and consequently in their difference $m = n_\uparrow - n_\downarrow$ being noninteger [59]. Even when dopants in WX_2 are fully polarized in the single-impurity limit, as is the case for V and Ti, their exchange splittings may be smaller than those in CrX_2 and MoX_2 (see Table IV). As we discussed above, the greater spatial extent of the W 5d orbitals leads to wider impurity bands for a given size of supercell. Similarly, the greater interaction between impurity states and host W d orbitals renders the impurity states more delocalized. For WX_2 doped with Nb and Ta, a larger supercell is needed to reach the single-impurity limit; in the present case, a magnetic moment of 1μ_B is found with a 15×15 supercell. The double acceptor impurities are all fully polarized with magnetic moments of 2 μ_B except for the disulphide MS_2 monolayers with M = Cr, Mo, W. In these systems, the a_1' levels lies well above the e' levels, as seen in Fig. 3 (rhs), leaving two holes to occupy the singly degenerate a_1' level with opposite spins and no magnetic moment. In the MSe$_2$ and MTe$_2$ monolayers, the holes are accommodated in doubly degenerate e' levels and can have the same spin. However, the half-filled orbitally degenerate state is susceptible to a Jahn-Teller (JT) distortion and there is a competition between exchange interaction and JT distortion. If the JT distortion is strong enough, the magnetic moment will be quenched. This will be discussed in Sec. III B 5.

TABLE IV. Exchange splittings Δ (in meV) calculated with a 12×12 supercell for monolayers of MX_2 in which a single M atom is replaced by V or Ti. Jahn-Teller distortion is included for single but not for double acceptors.

M		S			Se			Te	
M'	X	Cr	Mo	W	Cr	Mo	W	Cr	Mo
V	a_1'	34.5	96.1	91.2					
	e'	21.5	15.2	9.3	24.2	26.7	12.0	24.1	44.0
Ti	a_1'	0.0	0.0	0.0	71.3	86.5	93.8		
	e'	0.0	0.0	0.0	73.3	84.8	64.4	71.4	90.2

The exchange splittings Δ calculated for monolayers of MX_2 doped with V and Ti are listed in Table IV. The size of Δ depends on the spatial localization of the corresponding states, which in turn depends on the binding energies and orbital characters of the a_1' and e' levels. For V-doped MS_2 monolayers, the exchange splitting of the a_1' level is larger than that of the e' level because of its greater spatial localization. In V-doped MSe$_2$ and MoTe$_2$ monolayers, the a_1' levels overlap with the top of the valence band, Fig. 3, making it difficult to identify the corresponding exchange splittings, which are not given in Table IV. In the sequence $MS_2 \rightarrow M\mathrm{Se}_2 \rightarrow M\mathrm{Te}_2$, the exchange splittings of the e' levels are seen to increase (but not for CrSe$_2$:Ti → CrTe$_2$:Ti).

The exchange splittings of the Ti double acceptor levels are much larger than those of the V single acceptor because the impurity levels are much deeper and the hole densities much higher. As shown in Fig. 3, the e' impurity levels of double acceptors in MSe$_2$ are deeper than the a_1' levels making their wave functions more localized and their hole densities larger. Therefore, the exchange splittings of the e' levels are close to (or larger than) those of the a_1' levels, Table IV. In CrTe$_2$ and MoTe$_2$ monolayers, the a_1' levels are too shallow to be identified (Fig. 3) and the corresponding exchange splittings are not shown in the Table.

4. Symmetric relaxation

When a group VIB metal atom M in an MX_2 monolayer is substituted with a group IVB or VB element, the difference between the atomic radii of the dopant M' and host M atoms leads to a change in the bond length of the dopant with the neighboring chalcogen atoms. Symmetric structure relaxations that maintain the local D_{3h} symmetry of the dopant atom on the high-symmetry host site are found for all of the doped systems. For example, when a Mo atom in MoS$_2$ is replaced with a smaller V atom the surrounding S atoms move towards the V impurity causing the neighboring Mo atoms to move slightly away [8]. For the unrelaxed impurity, the a_1' and e' levels are essentially degenerate. The relaxation shifts the e' level slightly below the a_1' level as seen in Fig. 3 (and in Fig. 10 in [8]). The total energy gain of ~150 meV from the symmetric relaxation about an MoS$_2$:V impurity found in [8], is much larger than the gain of single-particle energy associated with the shift of the e' level indicating that a "defect molecule" picture [57] is greatly oversimplified. It is an order of magnitude larger than the energy gained from spin polarization. Similar behavior is found for Nb and Ta impurities, although because of their larger atomic radii the chalcogen atoms move away from them. The same pattern of symmetric relaxation appears in MoSe$_2$ but in the next subsection we will see that single acceptors in MoTe$_2$ exhibit an additional, nonsymmetric, Jahn-Teller, distortion.

The atomic volumes of the double acceptors Ti, Zr, and Hf are larger than those of Cr, Mo, and W and we find outward symmetric relaxations of the neighboring S ligands and transition metals in MS_2 monolayers, which are consistent with the ionic radii; these shift the e' levels much further below the a_1' level than happens for single acceptors, Fig. 3. When spin polarization is included simultaneously with relaxation for double acceptor-doped MSe_2 and MTe_2 monolayers, then the relaxation is found to be symmetric. Because of the large values of $\Delta_{K\Gamma}$ for MSe_2 and MTe_2 (Table I), the e' levels bound to the K/K' valley still lie above the a_1' levels bound to the Γ VBM after the symmetric relaxation, Fig. 3. The driving force for the symmetric relaxation is from the atomic interaction between the dopant and the atoms surrounding it and just as we found for single acceptors, the electronic energy gain is much larger than that associated with the (shallow) impurity levels in the gap. However, in some systems like V-doped $MoTe_2$ with partially occupied degenerate impurity levels, the energy gain from the splitting of degenerate impurity levels, the Jahn-Teller distortion, leads to additional atomic relaxation that we consider next.

5. Jahn-Teller distortions: Single acceptors

A substitutional impurity with partly filled, orbitally degenerate gap states satisfies the requirements of the Jahn-Teller (JT) theorem [60,61] and should undergo a symmetry-lowering distortion at sufficiently low temperature [57,62]. The distortion will split the partly-filled orbitally-degenerate level leading to a gain of single-particle energy that is linear in the amplitude x of the distortion whereas the elastic restoring force will be quadratic in x [63]. In equation form the JT energy E_{JT} can be written as

$$E_{JT}(x) = -F_{JT}\,x + \tfrac{1}{2}Kx^2 \qquad (2)$$

where F_{JT} is the force driving the JT distortion, $F_{JT}\,x$ is the energy gained by the symmetry lowering, and the elastic restoring force $-Kx$ depends on the strength of the bond between the dopant atom and the neighboring chalcogen atoms. In equilibrium, $x_0 = F_{JT}/K$ and the energy lowering is $\Delta E(x_0) = -F_{JT}^2/2K = -x_0 * F_{JT}/2$. If the harmonic response of the bonds to the displacement is stiff (large elastic constant K) and the e' orbitals are very delocalized (small F_{JT}), the JT distortion may be very weak resulting in a negligibly small displacement x_0. The situations for single (a) and double (b) acceptors with one, respectively, two holes in the e' level are sketched schematically in Fig. 4; the a_1' level is not shown. The displacement x leads to a splitting δ of the partly filled e' level that is linear in x. An exchange splitting Δ of the orbitally degenerate level that can compete with the symmetry lowering is included [64]. The distortion relevant for a substitutional impurity is the displacement of the dopant atom from the center of an MX_6 trigonal prism indicated in Fig. 5 with a red arrow; this lowers the original local point group symmetry from D_{3h} to C_{2v}. The dopant atom moves in the metal plane so mirror symmetry with respect to this plane is preserved.

For MoS_2, the small value of $\Delta_{K\Gamma}$ (Table I) makes the a_1' impurity levels bound to the Γ VBM accommodate the hole. Explicit tests in Ref. [8] showed that symmetry-lowering distortions were energetically unfavorable for single-acceptor-doped MoS_2 monolayers and only symmetric relaxation was found to occur. In view of the near degeneracy of the a_1' and e' levels and the finite dispersion of these states when modelled in a finite supercell, we could understand that an eventual energy gain in the single-impurity limit might be masked by the supercell approximation. However, for $MoSe_2$ and $MoTe_2$

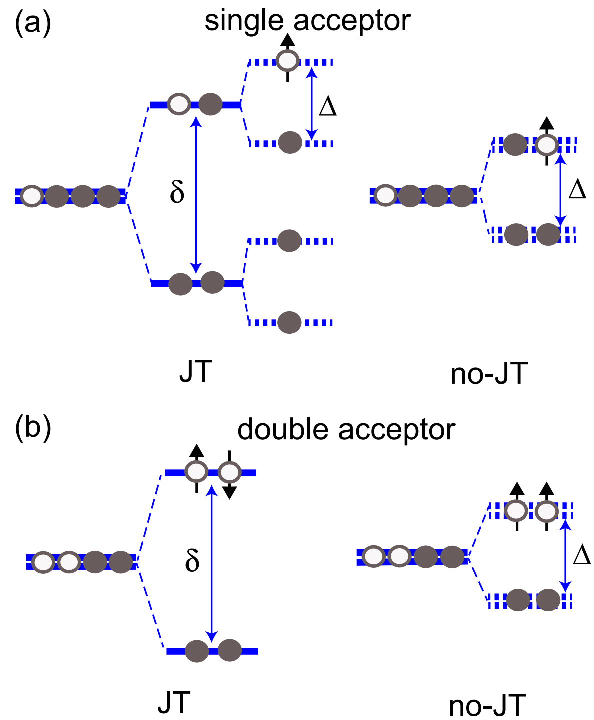

FIG. 4. Schematic of the energy gain with and without Jahn-Teller distortion for (a) single and (b) double acceptors. The solid and dashed blue lines represent spin-degenerate and spin-resolved energy levels, respectively. δ denotes the energy splitting of the degenerate e' levels caused by JT distortion and Δ is the exchange splitting. Solid and open circles denote electrons and holes, respectively. The completely filled (with electrons; empty of holes) a_1' level is not shown.

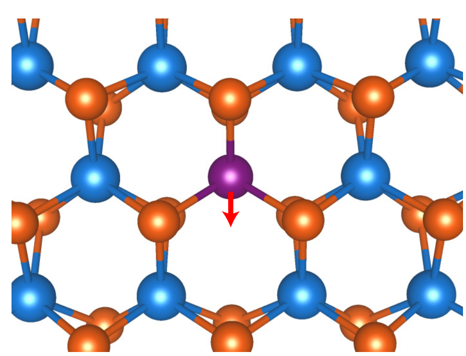

FIG. 5. Top view of the dopant-induced Jahn-Teller distortion in an MX_2 monolayer. The purple ball represents the dopant atom and the red arrow indicates its displacement for single acceptors; for double acceptors, the displacement is in the opposite direction. Because of the threefold symmetry of the unrelaxed structure, the symmetry-lowering dopant displacement can be in any one of three equivalent directions.

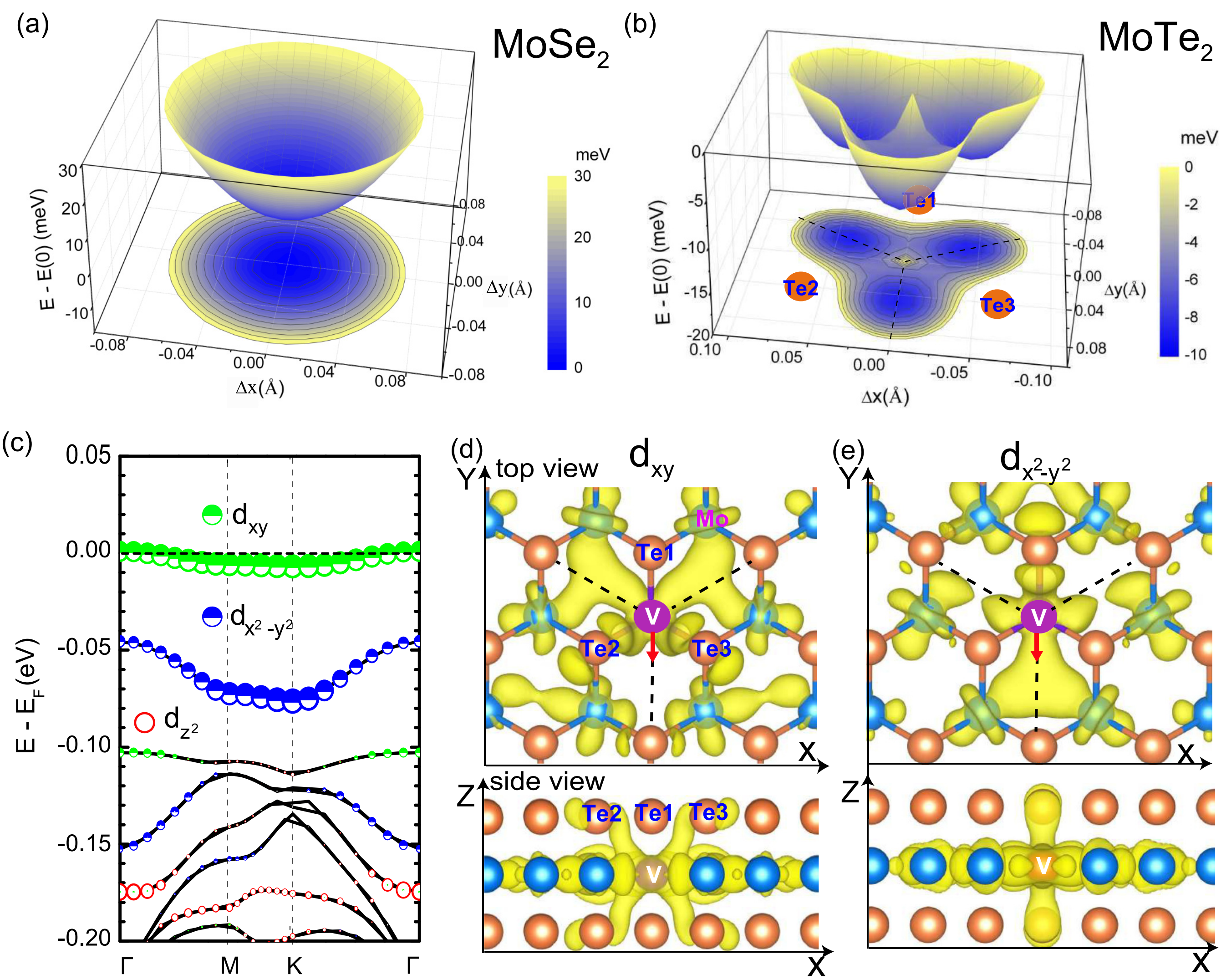

FIG. 6. Total energy on displacing a substitutional vanadium dopant V_{Mo} in the central *xy* metal plane away from the Mo lattice site in a 12×12 supercell of monolayers of (a) $MoSe_2$ and (b) $MoTe_2$ without allowing the host atoms to relax. Displacing the V atom along the dashed black lines in (b) weakens the V-Te_1 bonds while strengthening the V-Te_2 and V-Te_3 bonds. The brown circles in (b) represent the projection of the Te positions onto the metal plane. (c) Band structure without spin-polarization of the V-doped $MoTe_2$ monolayer for a 12×12 supercell with JT distortion corresponding to one of the minima in (b). The contributions from the vanadium d_{xy}, $d_{x^2-y^2}$ and d_{z^2} orbitals are shown as half-filled green, half-filled blue, and open red circles, respectively. Partial charge densities of the bands from (c) with d_{xy} (d) and $d_{x^2-y^2}$ (e) character with an isovalue of 0.001 e Å^{-3}. The red arrow indicates the displacement of the dopant atom (purple circle) when relaxed.

monolayers doped with single acceptors, the a_1' defect level lies well below the e' gap state, Table I. The latter contains a single hole and is therefore susceptible to a Jahn-Teller distortion [60,61]. However, no symmetry-lowering distortion is found for $MoSe_2$:V (vanadium-doped $MoSe_2$) while it does reduce the total energy for $MoTe_2$:V. To better understand what is happening, we examine these two cases in more detail by constructing the potential energy surfaces shown in Fig. 6 for (a) $MoSe_2$:V and (b) $MoTe_2$:V monolayers by calculating the total energy of a dopant V atom as a function of its displacement in the *xy* metal plane in a 12×12 supercell without allowing the host atoms to relax.

For the $MoSe_2$:V monolayer the potential minimum corresponds to an undisplaced, symmetric V dopant. The situation is unchanged and the D_{3h} symmetry maintained when the neighboring atoms are allowed to relax. The strong V-Se bond with significant hybridization of the V d_{xy/x^2-y^2} and Se *p* orbitals leads to a large elastic restoring force. The gain of electronic energy from the JT distortion fails to compensate the cost of elastic energy and no JT distortion is found for single-acceptor-doped $MoSe_2$ monolayers in calculations with the largest supercell we considered (12×12).

By contrast, the potential energy surface for the $MoTe_2$:V monolayer has three equivalent in-plane minima with the V atom displaced away from a pair of nearest-neighbor Te atoms above and below the Mo plane (Te_1 in Fig. 6) weakening the corresponding V-Te bonds. The JT distortion corresponding to this displacement of the dopant atom from the high-symmetry site breaks the local D_{3h} symmetry, lifts the degeneracy of the e' levels with d_{xy} and $d_{x^2-y^2}$ orbital character, Fig. 6(c), and lowers the energy. From the orbital-resolved band structure for $MoTe_2$:V shown in Fig. 6(c), we see that the impurity level with d_{xy} orbital character is raised by the JT distortion while the impurity level with $d_{x^2-y^2}$ orbital character is lowered. The partial charge densities of the bands with V d_{xy}, Fig. 6(d), and $d_{x^2-y^2}$, Fig. 6(e), orbital character show that the JT displacement of V away from Te_1 reducing the V-Te_2 and V-Te_3 bond lengths increases the hybridization between the V d_{xy} orbital and Te p orbitals and raises the impurity levels with d_{xy} orbital character. On the contrary, the band with $d_{x^2-y^2}$ orbital character is lowered by weakening the V-Te_1 antibonding interaction. As illustrated in Fig. 4(a), the JT distortion does not quench the magnetic moment but the symmetry breaking of the local structure does affect the exchange interaction between pairs of dopant atoms. This will be discussed in Sec. V.

For V-doped $MoTe_2$ monolayers, the V−Te bond is weaker than the V−Se bond [65] and our first-principles calculations yield a JT displacement of $x_0 = 0.04$ Å. The energy gained by the JT distortion is determined from the difference in energies of the JT distorted structure and of the same structure with the dopant returned to its initial high-symmetry position. The net energy gain is found to be $\Delta E(x_0) = 7$ meV. Using the simple model described by (2) according to which $\Delta E(x_0) = -F_{\rm JT}^2/2K = -x_0 * F_{\rm JT}/2$, we estimate $F_{\rm JT} \sim 0.014/0.04 = 0.35\,{\rm eV/Å}$ and $K \sim 0.35^2/0.014 = 8.75\,{\rm eV/Å}^2$.

In the MX_2 compounds, the bond strength (∼ elastic constant K) decreases as X goes from S to Te [65,66], making it more advantageous for the dopant to move from its original position. The lattice constant of $MoTe_2$ is larger than that of $MoSe_2$ that is in turn larger than that of MoS_2 so the impurity atom is in a larger cavity and presumably becoming less and less comfortable with this. The JT driving force described by $F_{\rm JT}$ is the single-particle-energy gained by breaking the degeneracy of the e' levels. We can understand our failure to observe a JT distortion for MoS_2:V and $MoSe_2$:V while finding one for $MoTe_2$:V in terms of the impurity bandwidth becoming smaller in the same order making the degeneracy lifting easier. For an unrelaxed, undisplaced substitutional V, the bandwidth of the e' impurity levels is found to decrease from 19.7 meV → 12.5 meV → 9.8 meV for S → Se → Te. $F_{\rm JT}$ increases and K decreases so that the JT distortion as described by (2) becomes more favorable in the same order.

To confirm the relationship between the impurity bandwidth and the JT distortion, we add an on-site Coulomb repulsion, $U - J = 5\,{\rm eV}$ [67] to the V-3d orbitals in the V-doped $MoSe_2$ monolayer. This pushes electrons from the V onto the neighboring atoms, localizing the hole on the V. The effective Bohr radius a_0^* is reduced from 6.9 Å to 5.3 Å, resulting in a reduced impurity bandwidth and an increased JT displacement of $x_0 = 0.07$ Å. Nb and Ta dopants behave just like V in that no JT distortion occurs for MoS_2 and $MoSe_2$ systems. The impurity bandwidths of the e' states obtained for Nb and Ta in $MoTe_2$ using a 12×12 supercell are larger than that found for V leading to a weaker JT distortion with a small displacement of only about 0.01 Å.

The modeling of single impurities with supercells is ultimately limited by the maximum supercell size that can be handled using the VASP (or any other) plane-wave code. In the single-impurity limit (infinite supercell size) the impurity levels become dispersionless and the localization of the impurity wavefunction increases the JT driving force facilitating the JT distortion; in the single-impurity limit the JT theorem must hold at $T = 0$ K.

Replacing S in MoS_2 with Se and Te leads to a substantial lowering of the Γ-point VBM with respect to the K-point VBM and a corresponding lowering of the defect state bound to the Γ VBM. The same is found to hold true for the Cr and W diselenides and ditellurides as seen in the increased value of $\Delta_{K\Gamma} = \varepsilon(K) - \varepsilon(\Gamma)$ in Table I and in the rapid descent of the a_1' states with respect to the e' states in Fig. 3. Just as we found for single acceptors in MoS_2, only a symmetric relaxation is found for single-acceptors in CrS_2 and WS_2. For $CrSe_2$, $CrTe_2$, and WSe_2 monolayers, no JT distortions are found. In some systems, which should be JT unstable, the large elastic constant and delocalized impurity wavefunctions prevent the JT distortion occurring when these systems are modelled using 12×12 supercells.

6. Jahn-Teller distortions: Double acceptors

In Sec. III B 2 we noted that for double acceptors (rhs of Fig. 3), the main trends for the a_1' and e' levels in MX_2 paralleled those found for single acceptors, the main difference being much larger impurity binding energies. For MS_2 monolayers, the a_1' levels were placed well above the e' levels and were occupied with the two holes introduced by Ti, Zr, and Hf doping. As a result there is no JT distortion and the relaxation is similar to that found for single acceptors. For MSe_2 and MTe_2 monolayers, the a_1' levels follow the Γ-point VBM down in energy losing their holes to the e' levels that, being half filled, are susceptible to Jahn-Teller distortion.

As suggested in Fig. 4(b), there is competition between JT distortion and spin polarization. If only symmetric relaxation is allowed with spin polarization, then the double acceptors polarize fully (rhs). However, if symmetry lowering is allowed, then the JT distortion quenches the magnetic moment (lhs). This indicates that two local minima exist that are close in energy: a JT state without spin polarization (lhs) and a spin-polarized state without JT distortion (rhs).

Which solution is found depends on how the DFT calculations are performed. If we start with a symmetrical configuration with both holes in a fourfold orbitally- and spin-degenerate state and first allow it to spin polarize, then the fourfold degenerate e' level splits into twofold up-spin and down-spin levels. The uppermost e' level is filled with the two holes and is no longer JT active; the dopant atom does not move and the local symmetry is not broken. If we start with an unpolarized state with a half filled spin-degenerate e' level, the impurity atom moves off center and the uppermost d_{xy} level is filled with an up-spin and a down-spin hole and cannot spin polarize. Apart from the position of the dopant atom itself, the relaxed local atomic geometries with spin polarization (SP) and without (JT state) are almost identical. Assuming the same symmetric relaxation around the dopant and correspondingly, the same energy gain, then we can model the total energy as

$$E_{\rm SP} = E_0 - E_{\rm sym} - E_\Delta, \tag{3}$$

$$E_{\rm JT}(x_0) = E_0 - E_{\rm sym} - F_{\rm JT}\, x_0 + \tfrac{1}{2} K x_0^2, \tag{4}$$

TABLE V. Calculated net energy gain ΔE in meV of the JT state with respect to the spin-polarized state for double-acceptor-doped MX_2 (M = Cr, Mo, W; X = Se, Te) monolayers.

	M	Se			Te	
M'	X	Cr	Mo	W	Cr	Mo
Ti		54	–45	–10	42	–90
Zr		70	–11	–6	56	–82
Hf		76	–12	–5	59	–80

respectively, in which E_{sym} and E_Δ represent the energy gain from the symmetric relaxation and exchange splitting, respectively. E_0 is the total energy without relaxation and spin polarization while x_0 represents the equilibrium displacement of the dopant atom.

For single acceptors in $M\text{Se}_2$ and $M\text{Te}_2$ monolayers, the JT distortion does not compete with spin polarization as sketched in Fig. 4. For double acceptors with two holes, only singlet states are compatible with lifting of the orbital degeneracy of the e' levels. The net energy gain of the JT state with respect to the spin-polarized state is

$$\Delta E = E_{\text{JT}}(x_0) - E_{\text{SP}} = -F_{\text{JT}}\, x_0 + \tfrac{1}{2}Kx_0^2 + E_\Delta. \qquad (5)$$

The impurity states delocalize on going from Ti to Hf leading to a weaker driving force F_{JT} and so a smaller stabilization energy ΔE as listed in Table V. In double-acceptor-doped $MoSe_2$, $MoTe_2$, and WSe_2 monolayers, the JT distorted state is more favorable than the spin-polarized solution with negative values of ΔE. As discussed above, a $MoTe_2$ monolayer has a relatively small K and large F_{JT} compared to a $MoSe_2$ monolayer. As a result, (ΔE and x_0) are quite large in a double-acceptor-doped $MoTe_2$ monolayer: Ti (–90 meV, 0.11 Å) and Hf (–80 meV, 0.11 Å). A WSe_2 monolayer has a large elastic constant $K \sim 147$ N/m [66] (9.2 eV/Å^2), resulting in a small value of ΔE: -10 meV for Ti and -5 meV for Hf. It should be noted that the direction of the JT displacement for double acceptors is opposite to that of single acceptors.

The structural relaxation in doped $\text{Cr}X_2$ and $\text{W}X_2$ monolayers is similar to that in $\text{Mo}X_2$. In double-acceptor-doped $CrSe_2$ and $CrTe_2$, the e' states are quite shallow (see rhs of Fig. 3) and correspondingly delocalized, which leads to a weak JT driving force F_{JT}. The a_1' levels that are close to the e' levels broaden into impurity bands in the supercell approximation, see e.g., Fig. 6(c), and become partially populated with holes. This increases E_Δ because of the larger exchange splitting of the a_1' levels. When this happens, ΔE becomes positive indicating that spin-polarized states are energetically more favorable than JT states.

7. Single ion anisotropy

For the isotropic 2D Heisenberg model with a gapless spin-wave spectrum, thermal fluctuations at any finite temperature will destroy long-range magnetic ordering whereas the magnetic anisotropy implicit in the 2D Ising model makes the system undergo a phase transition at a finite temperature to a magnetically ordered state [15,16]; magnetic anisotropy is essential for long-range ferromagnetic ordering in two dimensions. For the recently reported ferromagnetic CrI_3 [68] and Fe_2GeTe_3 [69,70] monolayers, single ion anisotropy (SIA) plays an important role in stabilizing the long-range order [69,71]. We can expect the same to hold for MX_2 monolayers doped to make them magnetic, making it important to determine their magnetic anisotropy. We will study this in the single-impurity limit.

To be able to interpret the SIA calculated from first-principles, we consider the model Hamiltonian for the doped system including spin-orbit coupling (SOC) and spin polarization

$$H = H_0 + \Delta\mathbf{m}\cdot\mathbf{s} + \xi\mathbf{l}\cdot\mathbf{s} \qquad (6)$$

in which H_0 is the spin-independent part of the Hamiltonian, $\Delta\mathbf{m}$ is the exchange field that leads to an exchange splitting Δ, $\mathbf{m}$ is a unit vector in the direction of the magnetization, $\mathbf{m} \equiv \mathbf{M}/|\mathbf{M}|$, and ξ is the conventional spin-orbit coupling parameter. In the subspace of the $l = 2$, $m_l = \pm 2$ orbitals

$$\xi\mathbf{l}\cdot\mathbf{s} = \frac{\xi}{2}\begin{pmatrix} l_z & l_- \\ l_+ & -l_z \end{pmatrix} = \begin{pmatrix} \xi & 0 \\ 0 & -\xi \end{pmatrix} \qquad (7)$$

where we use Hartree atomic units with $\hbar = 1$. For $\mathbf{M} \parallel c$,

$$\Delta\mathbf{m}\cdot\mathbf{s} = \begin{pmatrix} \frac{\Delta}{2} & 0 \\ 0 & -\frac{\Delta}{2} \end{pmatrix}, \qquad (8)$$

and the SOC Hamiltonian can be written as

$$H = H_0 + \begin{pmatrix} \xi + \frac{\Delta}{2} & 0 & 0 & 0 \\ 0 & -\xi - \frac{\Delta}{2} & 0 & 0 \\ 0 & 0 & -\xi + \frac{\Delta}{2} & 0 \\ 0 & 0 & 0 & \xi - \frac{\Delta}{2} \end{pmatrix}. \qquad (9)$$

Rotating the spin quantization direction from c to a we get for $\mathbf{M} \parallel a$,

$$H = H_0 + \begin{pmatrix} \xi & \frac{\Delta}{2} & 0 & 0 \\ \frac{\Delta}{2} & -\xi & 0 & 0 \\ 0 & 0 & -\xi & \frac{\Delta}{2} \\ 0 & 0 & \frac{\Delta}{2} & \xi \end{pmatrix}. \qquad (10)$$

Diagonalizing H results in the energy level scheme sketched in Fig. 7. Occupying these levels as appropriate for single and double acceptors results in the total energies E_c and E_a for $\mathbf{M} \parallel c$ and $\mathbf{M} \parallel a$, respectively, from which the single ion anisotropy energy $E_{\text{MAE}} = E_a - E_c$ can be estimated to be

$$E_{\text{MAE}} = \begin{cases} \xi + \frac{\Delta}{2} - \sqrt{\xi^2 + \frac{\Delta^2}{4}} & \text{for V, Nb, Ta} \\ 2\xi - \sqrt{4\xi^2 + \Delta^2} & \text{for Ti, Zr, Hf} \end{cases} \qquad (11)$$

where positive values favor an out-of-plane spin orientation and negative values in-plane. Equation (11) shows how the SIA depends on both the SOC and exchange interaction. It is clear that single acceptors yield positive values; double acceptors yield negative values (if the magnetic moments are not quenched by a JT distortion on iterating to self-consistency).

We calculated the SIA numerically from first principles using the force theorem [72,73], which expresses the difference between two total energies as the difference in the sum of Kohn-Sham eigenvalues [74] for $\mathbf{M} \parallel a$ and $\mathbf{M} \parallel c$ [75].

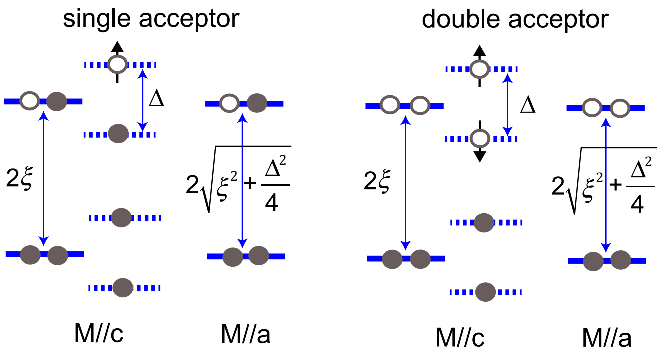

FIG. 7. Schematic diagram of the energy gain with spin orientation in-plane ($\mathbf{M} \parallel a$) and out-of-plane ($\mathbf{M} \parallel c$) for single and double acceptors. The solid and dashed blue lines represent spin degenerate and spin resolved levels, respectively. Solid and open circles denote electrons and holes, respectively.

Table VI compares the SIA from (11) with the first-principles results. We note that the spin-orbit splitting of the e' levels for the V-doped MoS_2 monolayer is similar (130 meV) to that of the K/K' VBM of a pristine MoS_2 monolayer, while the a_1' level has no spin-orbit splitting just as the Γ valley of the MoS_2 monolayer has none. The exchange splitting is 15.2 meV and 96 meV for the e' and a_1' levels, respectively. In Table VI, we see an estimate of 7.2 meV using (11), larger than what we calculate from first principles, 4.5 meV. We note that because of the near degeneracy of the a_1' and e' levels and the impurity band dispersion in a supercell approximation, the a_1' level may accommodate some of the hole. This does not contribute to the SIA, leading to the first-principles SIA being smaller than that estimated using (11) that does not take this factor into account. In addition, because the e' level has become a band with a finite dispersion, the energy gain from the exchange splitting Δ will be reduced, which will also reduce the SIA. The values from (11) are a simple estimate of the SIA in the single-impurity limit with all holes in e' states. For all of the systems in Table VI there is reasonable

TABLE VI. Calculated spin-orbit splitting 2ξ, exchange splitting Δ, single ion anisotropy (SIA) in meV, and effective Bohr radius a_0^* in Å for the degenerate e' levels in monolayers of MX_2 (12×12 supercell) doped with V and Ti substituting a single Mo. The SIA estimated from (11) is also shown for comparison. The atomic structures are fully relaxed with spin polarization.

M		S			Se			Te	
X		Cr	Mo	W	Cr	Mo	W	Cr	Mo
V	2ξ	66	130	187	78	107	181	91	110
	Δ	21.5	15.2	9.3	24.2	26.7	12.0	24.1	44.0
	SIA: (11)	9.0	7.2	4.5	10.3	11.0	5.8	10.5	17.8
	SIA:DFT	4.7	4.5	3.2	7.2	10.0	4.7	7.7	11.2
	a_0^*	8.3	8.0	8.8	8.9	6.9	9.4	9.3	6.4
Ti	2ξ	0.0	0.0	0.0	78	87	148	83	105
	Δ	0.0	0.0	0.0	13.3	84.8	64.4	71.4	90.2
	SIA: (11)	0.0	0.0	0.0	–1.1	–34.4	–13.4	–26.4	–31.1
	SIA:DFT	0.0	0.0	0.0	–0.3	–24.1	–5.2	–23.4	–25.5

TABLE VII. Calculated formation energy in eV of a chalcogen vacancy $\O_X$, a transition metal vacancy $\O_M$, and an M_X antisite (one transitional metal atom occupying a chalcogen atom site) in a MX_2 monolayer including relaxation.

M	S			Se			Te	
X	Cr	Mo	W	Cr	Mo	W	Cr	Mo
$\O_X$	2.47	3.15	3.01	2.46	2.77	2.72	2.26	2.89
$\O_M$	6.31	7.87	7.27	4.80	6.04	5.85	2.44	4.60
M_X	4.72	6.71	7.12	4.44	5.51	6.48	3.31	4.61

qualitative agreement between the DFT supercell calculations and the SIA estimate of Eq. (11).

In the limit $\Delta \ll \xi$, $E_{\mathrm{SIA}} \sim \frac{\Delta}{2}(1 - \frac{\Delta}{4\xi})$ for single acceptors and the SIA depends mainly on the exchange splitting Δ. In $MoSe_2$, the SIA can be as high as 10 meV/dopant, larger than the 4.5 meV/dopant in MoS_2. V in $MoTe_2$ has a very large exchange splitting but because of the JT distortion, the SIA is not as high as the value estimated from (11). Pristine WS_2 and WSe_2 monolayers have a large spin-orbit splitting of the K/K' valley ($\sim$ 0.4–0.6 eV), but the splitting of the impurity levels in these systems is only half of these values. The more delocalized the holes become, the smaller is Δ and consequently the SIA. In CrX_2 monolayers, the impurity states have a large exchange splitting Δ but the small SOC leads to SIA values intermediate between those found for MoS_2 and WS_2.

C. Interaction with intrinsic defects

Intrinsic defects like vacancies and antisite defects are ubiquitous in van der Waals materials and have been investigated in many experimental [76–78] and computational [79–81] studies. We denote vacancies on M and X sites as $\O_M$ and $\O_X$, respectively. Analogously, antisite defects are denoted A_B for an A atom on a B site; thus, in the present case we will be concerned with M_X. The formation energies of the various defects listed in Table VII are defined as

$$E_{\mathrm{form}}[\mathrm{def}] = E_{\mathrm{tot}}[MX_2 : \mathrm{def}] - \left(E_{\mathrm{tot}}[MX_2] - \sum_{\alpha} n_\alpha \mu_\alpha\right) \tag{12}$$

where $E_{\mathrm{tot}}[MX_2 : \mathrm{def}]$ and $E_{\mathrm{tot}}[MX_2]$ denote total energies of supercells containing a defect and of the perfect material, respectively; n_α is the number of atoms added or removed and μ_α ($= \mu_M$ or μ_X) represents the corresponding M or X chemical potential in their bulk phases (bcc or hexagonal phase for M atoms; monoclinic or triclinic phase for X atoms). The formation energy of a chalcogen X atom vacancy $E[\O_X]$ is about half that of a transition metal vacancy $E[\O_M]$, or half that of an antisite defect with a metal atom on an X site $E[M_X]$, indicating that chalcogen vacancies are more likely to be formed in thermodynamic equilibrium than the other two defects. The formation energies $\O_M$ and M_X are fairly close in value and decrease from MS_2 to MTe_2. Compared to the formation energy of acceptors (see Table II), much more energy is required to form intrinsic defects. This suggests

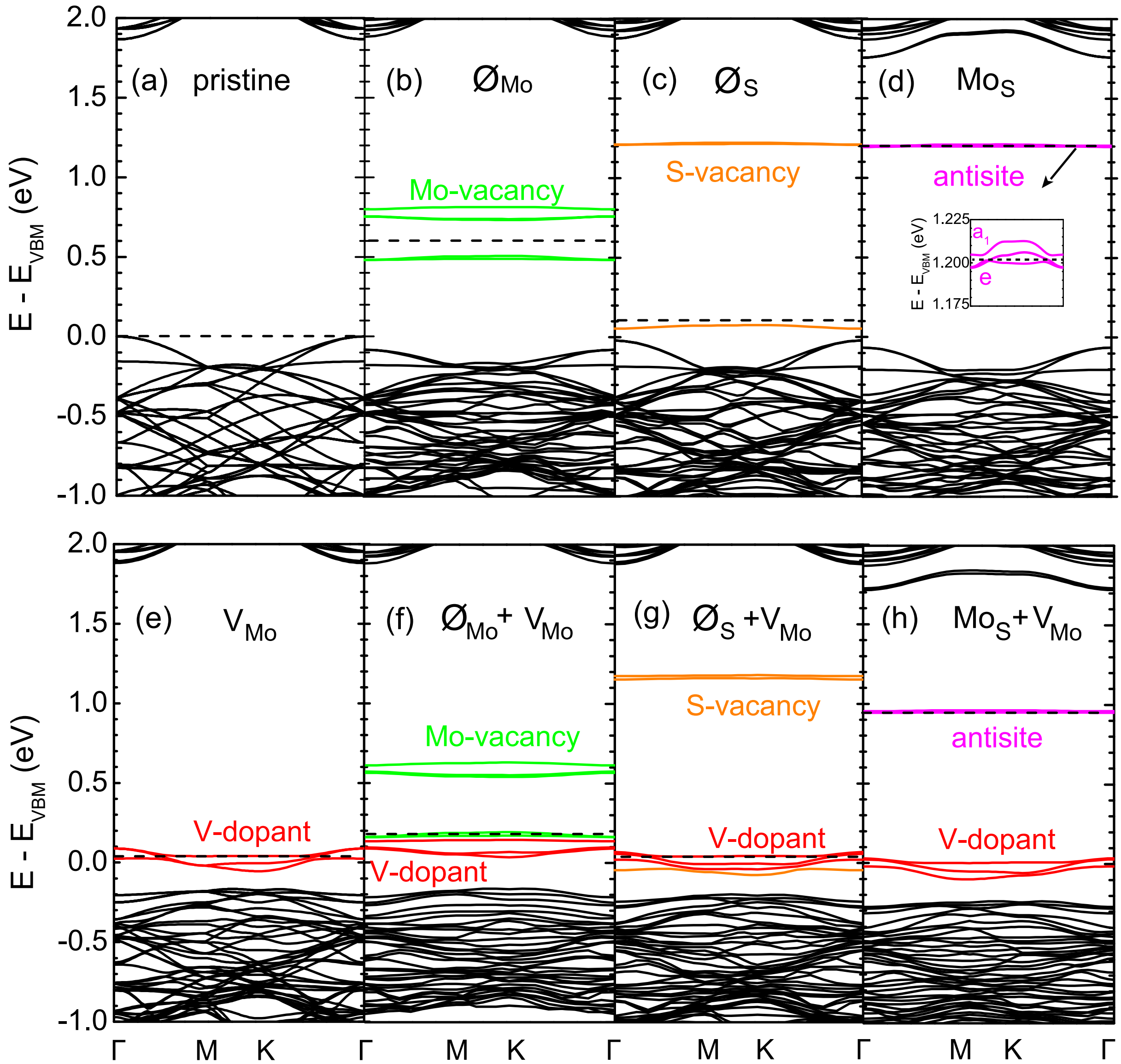

FIG. 8. Band structures for (a) a defect-free MoS_2 monolayer, (b) a Mo vacancy $Ø_{Mo}$, (c) a sulfur vacancy $Ø_{Mo}$, (d) a Mo_S antisite defect consisting of a Mo atom on a S site, (e) a vanadium atom on a Mo site V_{Mo}, (f) a Mo vacancy next to a substitutional vanadium atom $Ø_{Mo} + V_{Mo}$, (g) a sulfur vacancy next to a substitutional vanadium atom $Ø_S + V_{Mo}$, (h) a Mo_S antisite defect next to a substitutional vanadium atom $Mo_S + V_{Mo}$ all modelled for MoS_2 with a 6×6 supercell. The zero of energy is the top of the valence band, which is not always visible in a finite supercell; its determination is discussed in [8]. The Fermi level is indicated by a dashed black line. The inset in (d) is a blow-up of the band structure near the Fermi level.

that in order to suppress the formation of intrinsic defects, acceptors should be incorporated into MX_2 monolayers at low temperatures.

Just as substituting a Mo atom with an acceptor (single or double) leads to the formation of states in the fundamental bandgap, Figs. 3 and 8(e), defect states associated with a variety of intrinsic defects appear in the bandgap and can interact with those introduced by p doping. This is illustrated in Fig. 8 for an MoS_2 monolayer where the nonspin-polarized band structures for a number of intrinsic defects and complexes of intrinsic defects and adjacent substitutional V dopant atoms V_{Mo} are plotted. For simplicity, the structures are not relaxed and the effect of relaxation is discussed in the text.

A Mo vacancy $Ø_{Mo}$ with a formation energy of 7.87 eV introduces five midgap states, one singly degenerate state and two doubly degenerate states under local D_{3h} symmetry as shown in Fig. 8(b). Six holes are hereby introduced into the system that occupy the three defect states above the Fermi level. Structural relaxation preserves the D_{3h} symmetry as expected from the absence of partially occupied orbitally degenerate states. However, the relative position of the deep defect states depends on the particular system under consideration. For example, for a $MoTe_2$ monolayer with a Mo vacancy, the singly degenerate state lies far below the doubly degenerate states so that the Fermi level lies in the doubly degenerate states leading to a JT distortion.

A sulfur vacancy $Ø_S$ with a formation energy of 3.15 eV, introduces three gap states: an orbitally doubly degenerate, unoccupied midgap state and a fully occupied singly degenerate state close to the VBM, Fig. 8(c). Usually a sulfur vacancy is considered to be an electron donor but for that to be true, the occupied state would have to be close to the CBM, which is not the case. There are no partially filled defect states so that structural relaxation preserves the C_{3v} site symmetry. The Mo atoms surrounding the S vacancy move towards it which raises the occupied $Ø_S$ defect state slightly in energy. This is true for all MX_2 monolayers and chalcogen vacancies do not introduce spin-polarization or induce JT distortions.

A Mo_S antisite consists of a sulfur vacancy occupied by an extra Mo atom. The S vacancy removes two holes while the Mo atom contributes six electrons, Fig. 8(d). Four of these electrons are accommodated in the sulfur vacancy midgap states that are pulled down into the valence band by the attractive Mo potential leaving two electrons in a deep doubly degenerate e state under the local C_{3v} symmetry that is quasidegenerate with an a_1 singlet and giving rise to a magnetic moment of 2 μ_B. The inset of Fig. 8(d) is a blowup of the band structure near the Fermi level. For the partially occupied degenerate e levels, JT distortion could lift the degeneracy but is not strong enough to do so and spin polarization prevails. The exchange-splitting of the doubly degenerate antisite states is 0.33 eV. For an $MoTe_2$ monolayer, relaxation lowers the a_1 level well below the e levels. The a_1 level accommodates both electrons so that an Mo_{Te} antisite is nonmagnetic.

As discussed in detail in Ref. [8], a vanadium atom on a Mo site V_{Mo} induces three shallow impurity-like levels above the VBM, which are shown unrelaxed in Fig. 8(e). With relaxation, we see these levels with binding energies of about 60 meV in Fig. 3. The intrinsic defect states shown in Figs. 8(b)–8(d) have very deep gap states (> 0.5 eV), indicating that the defect potential is effectively more repulsive for holes than the substitutional V dopant. If we introduce a Mo vacancy next to a V dopant ($Ø_{Mo} + V_{Mo}$), the V_{Mo} hole will transfer to the S atoms surrounding the Mo vacancy. As shown in Fig. 8(f), the hole goes into the lowest lying doubly degenerate $Ø_{Mo}$ defect state and polarizes fully; this might suppress the quenching of the magnetic moment we found for close V dopant pairs in Ref. [8].

A sulfur vacancy $Ø_S$ has one fully occupied defect state that is very close to the VBM, Fig. 8(c). When $Ø_S$ and V_{Mo} defects are neighbors, the shallow quasidegenerate defect states hybridize leading to a spatial redistribution of the hole, see Fig. 8(g). It should be noted that the defect states of $Ø_S$ mainly consist of Mo d states on the three Mo atoms that surround the S vacancy. The hybridization between V and Mo d orbitals enhances the magnetism as evidenced by an increased exchange splitting. When allowed to relax, the two Mo atoms and the V dopant adjacent to the S vacancy move towards the vacancy site. This inward shift enhances the hybridization of the V_{Mo} and $Ø_S$ defect states increasing the exchange splitting of the corresponding a_1' levels in a 6×6 supercell from 72 meV to 93 meV.

For a vanadium atom on a Mo site next to a Mo atom on a S site, a $Mo_S + V_{Mo}$ complex defect, the hole introduced by V_{Mo} moves to the partially filled Mo_S midgap states, resulting in a net magnetic moment of 1μ_B on the antisite Mo atom. The V dopant gets one extra electron from the antisite defect, which quenches its magnetic moment. When relaxation is included, a JT distortion appears for the partially filled degenerate defect states of the antisite but the complex remains spin polarized.

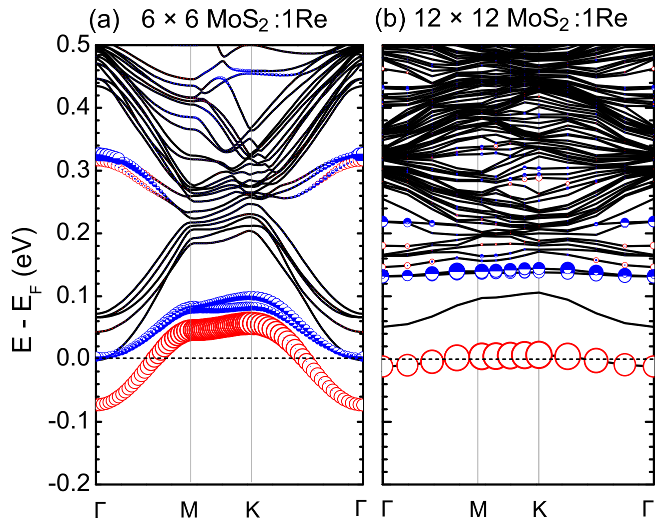

FIG. 9. Orbital resolved band structure of an MoS_2 monolayer with one Mo atom replaced with a Re atom in a (a) 6×6 and (b) 12×12 supercell. The open red circles and half-filled blue circles represent the contributions from Re $d_{3z^2-r^2}$ and $d_{x^2-y^2}, d_{xy}$, respectively. The Fermi level is indicated by the black dashed line.

All of the intrinsic defects we have examined are quite localized. Even though the local spin polarization can be enhanced by hybridization between intrinsic defects and dopant states in the sense that the exchange splitting is increased, this is unlikely to extend the range of the exchange interaction between magnetic defects. It has been reported that the existence of S vacancies might reduce the barrier for dopant diffusion [82]. This might allow dopants to migrate and more easily form pairs in the presence of S vacancies, which could lead to an enhanced ordering temperature at low doping concentration.

D. Electron doping: Rhenium

So far we have only considered the case of hole doping. Here we briefly consider the case of electron doping with the 5d element rhenium that gives rise to an attractive Coulomb potential in the single-impurity limit. We expect the electron-doping case to be more complex because according to Fig. 1 the conduction band minima (CBM) at K/K' will give rise to two degenerate states while the six Q point minima between K and Γ will give rise to an additional six degenerate states that will be coupled in degenerate perturbation theory by the Coulomb potential. In the effective mass approximation, the intervalley scattering between the K and K' valleys and the sixfold Q valleys leaves a single a_1' level with $d_{3z^2-r^2}$ character and a doubly degenerate e' level with mixed $\{d_{x^2-y^2}, d_{xy}\}$ character below the CBM as indicated in Fig. 9 with a binding energy of 92 meV. The lowest lying a_1' state polarizes fully in the single-impurity limit. In spite of its out-of-plane $d_{3z^2-r^2}$ character, the exchange splitting is weak (46 meV). This is manifested in the large dispersion of the a_1' level seen in Fig. 9. The small SOC at the CBM of MoX_2 monolayers leads to a negligible SIA. For WX_2 monolayers, it is relatively large compared to MoX_2 [40,42,83,84] leading to a large SIA of ∼10 meV/dopant. However, as we found for pairs of substitutional V atoms in a MoS_2 monolayer [8], below a critical separation the magnetic moment is quenched by a strong π bond being formed between Re pairs.

IV. RESULTS: PAIR INTERACTIONS

For semiconductors like the MX_2 transition metal dichalcogenides, the electronic structure of substitutional dopants from neighboring columns of the periodic table can be qualitatively understood within the framework of effective mass theory. We have confirmed this for M substitutions using DFT-based supercell calculations once the supercell size is sufficiently large to approach the single-impurity limit. For MoS_2 and WS_2 monolayers doped with single acceptors, the small energy difference $\Delta_{K\Gamma}$ between the K/K' and Γ valence band maxima means that the hole occupies the a_1' level bound to the Γ valley. For pairs of dopant atoms that are sufficiently close, the magnetic moment is quenched by the formation of singlet bonding states [8]. This quenching can be avoided by instead using MSe$_2$ and MTe$_2$ with M = Cr, Mo, W, which have larger values of $\Delta_{K\Gamma}$, see Table I; even the slightly larger value of $\Delta_{K\Gamma}$ for CrS_2 is enough to suppress it. Nevertheless, in order to realize long range and strong exchange interactions at high temperatures, the impurity states should have large effective Bohr radii as well as large exchange splittings, requirements, which are incompatible. The SIA of single acceptors also requires a large exchange splitting while double acceptors are excluded because of their in-plane anisotropy. In this section, we briefly consider the opportunities for realizing ferromagnetic ordering in the vanadium-doped systems considered in the previous sections.

Increasing the concentration of V doping increases the impurity bandwidth so the holes become more delocalized and the exchange splitting and MAE are reduced. This makes it more difficult for the Hund's-rule like alignment of spins to win the competition with the kinetic energy or for the MAE to win against thermal disorder. The effective Bohr radii a_0^* of the e' impurity states resulting from doping MX_2 with vanadium that are given in Table VI should be a measure of the range of the exchange interaction. The small values for $MoSe_2$ and $MoTe_2$ argue against their suitability as room-temperature ferromagnets. If we use the limiting case of the single-site exchange splitting Δ as a measure of the robustness of the magnetic moment to the adverse effects of temperature [64], then Table VI shows that V-doped CrS_2, $CrSe_2$, $CrTe_2$, $MoSe_2$, and $MoTe_2$ have reasonably large values. Small values of Δ make the stabilization of parallel and antiparallel configurations of two spins difficult (and computationally expensive) in a SCF calculation and we do not consider WS_2 or WSe_2 any further; MoS_2 was examined in detail in [8]. (In terms of its Bohr radius, WSe_2:V might look very promising and indeed it has been reported to exhibit ferromagnetic ordering at room temperature [23,24] but not in terms of its intraatomic or interatomic exchange interactions that are weak. We will discuss it separately in Sec. V.)

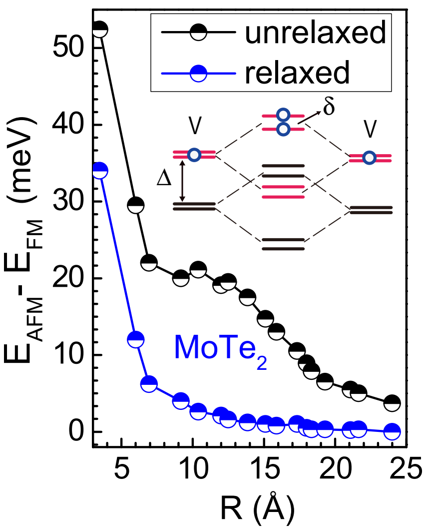

FIG. 10. Difference between the total energies of antiferromagnetic and ferromagnetic states for pairs of substitutional V impurities in 12×12 supercells plotted as a function of their separation for $MoTe_2$ monolayers with (half-filled blue circles) and without (half-filled black circles) relaxation. The solid lines are a guide to the eye. The inset shows the spin resolved bonding antibonding levels of ferromagnetically coupled V pairs in which red and black lines represent different spin channels. Δ represents the exchange splitting of the impurity states and δ the splitting of the degenerate e' levels as the V impurities get closer and interact. Open circles denote the holes.

Of the TMD monolayers considered in Table VI, V-doped $MoTe_2$ has the largest exchange splitting with $\Delta = 44$ meV and we expect the single site magnetic moment to be robust against the influence of temperature and the interaction with other dopant impurities when the V concentration is increased. To gauge the latter, we consider the exchange interaction between pairs of V dopants separated by lattice vectors **R** by calculating the total energy difference between ferromagnetically and antiferromagnetically ordered states of V pairs in 12×12 supercells, with and without relaxation as shown in Fig. 10. By mapping this energy difference onto a Heisenberg model, Monte Carlo calculations can be used to estimate ordering temperatures [8].

In the absence of relaxation, the hole of each individual V impurity occupies an orbitally doubly degenerate e' state, Fig. 3, that is exchange split by the amount Δ when spin polarization is allowed [64], as sketched in the inset to Fig. 10. Pairs of these V impurities exhibit a strong and long-range FM exchange coupling with points of inflection at separations of ∼7 Å and ∼14 Å between which the exchange energy flattens out, Fig. 10. At large separations, the doubly degenerate e' states form bonding-antibonding pairs with the holes gravitating to the highest-lying antibonding level (see the inset to Fig. 10); because of the orbital degeneracy, the spins can form a triplet corresponding to ferromagnetic coupling. Bringing the impurity pairs closer breaks the C_{3v} rotational symmetry upon which the twofold degeneracy of the e' levels is based and leads to a splitting δ of these levels. For separations between 14 Å and 7 Å, δ increases from approximately 3 to

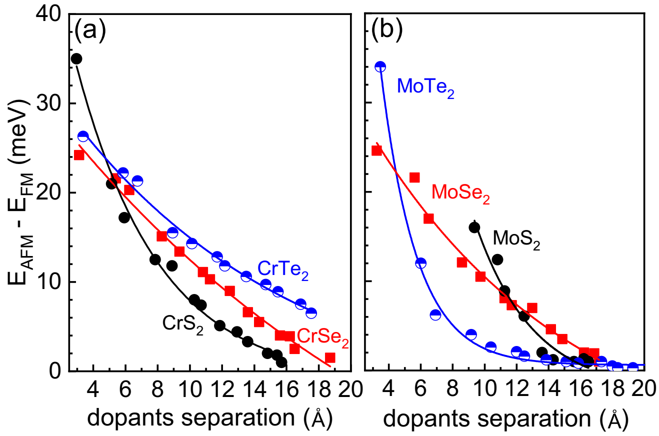

FIG. 11. Difference between the total energies of antiferromagnetic and ferromagnetic states for pairs of substitutional V impurities including relaxation in 12×12 supercells plotted as a function of their separation for (a) CrX_2 and (b) MoX_2 (X= S, Se, Te) monolayers. The solid lines are a guide to the eye.

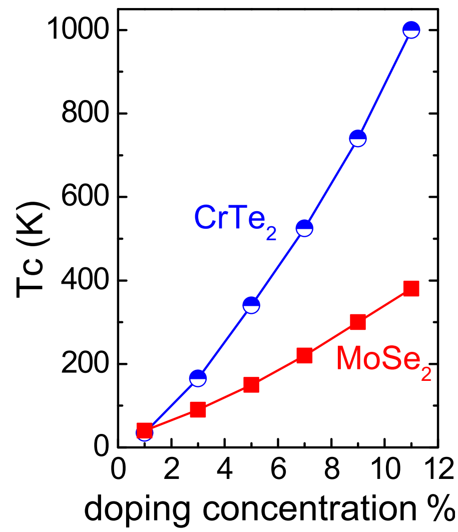

FIG. 12. Curie temperature as a function of doping concentration for V-doped $MoSe_2$ (red square) and $CrTe_2$ (blue half-filled circle) monolayers.

7 meV. This leads to a reduction in the exchange interaction between V pairs, which is evident in the formation of a plateau at separations between approximately 7 Å and 14 Å. At short separations, the bonding-antibonding interaction between d_{xy} and $d_{x^2-y^2}$ orbitals on V neighbors and the exchange splitting Δ of the impurity states are much larger than δ, the symmetry breaking of the e' level. Thus, as the dopants get closer ($<$ 7 Å), the exchange interaction increases steeply.

When relaxation is included, the JT distortion lifts the degeneracy of the partly filled e' levels as shown in Fig. 6(c) suppressing the preference for triplet states. As well as leading to the reduced MAE we found in Sec. III B 5, this greatly reduces the interatomic exchange interaction making it effectively much shorter range than expected on the basis of the Bohr radius for a single dopant impurity. One possibility to circumvent this would be to consider doping a $Mo(Se_xTe_{1-x})_2$ substitutional alloy with V; this, however, goes beyond the scope of the present paper.

The interatomic exchange interaction in the MoX_2 system, shown in Fig. 11(b), is quite complex because of (i) the magnetic quenching in MoS_2 discussed at length in Ref. [8] and (ii) the JT effect in $MoTe_2$ discussed in the previous paragraph. While the JT distortion makes the exchange interaction of $MoTe_2$ very short ranged, in MoS_2 the magnetic moment is quenched for V pairs below a critical separation (∼9 Å). In the intermediate Se case, our calculations found the JT distortion to be negligible for a single impurity and $MoSe_2$:V shows a relatively strong and long-range exchange interaction.

For relaxed V pairs in CrX_2 monolayers, the ferromagnetic-antiferromagnetic energy difference is plotted as a function of the separation R in Fig. 11(a) where the exchange interaction is seen to decay more slowly and gets stronger in the sequence $CrS_2 \rightarrow CrSe_2 \rightarrow CrTe_2$. Even though the Bohr radius of e' levels in V-doped CrS_2 is 8.3 Å, the exchange interaction drops faster with dopant separation than in $MoSe_2$, which has a smaller effective Bohr radius. This is because the a_1' level in V-doped CrS_2 is so close to the e' levels (see Fig. 3) that are therefore only partly occupied, as we originally found for V-doped MoS_2 [8]. A key difference is that the a_1' level in the V-doped CrS_2 monolayer is not high enough to quench the magnetic moment for even the closest dopant pair separation. It should be noted that in CrS_2, $CrSe_2$, $CrTe_2$, and $MoSe_2$ the JT distortions are negligible so the doubly degenerate impurity levels remain degenerate and the exchange interactions do not change much with relaxation.

According to the results shown in Fig. 11, V-doped $CrTe_2$ and $MoSe_2$ exhibit the longest range exchange interactions of all the systems we have studied. We use the same Monte Carlo methodology as used for MoS_2:V in Ref. [8] to estimate their Curie temperatures (T_C) and plot these as a function of the vanadium concentration x in Fig. 12(b). Room-temperature values of T_C are predicted for $MoSe_2$ and $CrTe_2$ monolayers for V dopant concentrations of 9% and 5%, respectively. In view of the comparable magnitude of the exchange interaction between very close V dopant pairs for $CrTe_2$ and $MoSe_2$, the longer range of the exchange interaction in $CrTe_2$ is pivotal in achieving RT ferromagnetism for low dopant concentrations.

V. DISCUSSION

We have explored how the magnetization of hole-doped MX_2 monolayers depends on the interplay of the exchange interaction of pairs of impurities with the exchange splitting [64], JT distortion and magnetic anisotropy of single impurities. The fundamental conundrum in the quest for a high-temperature magnetic semiconductor is the incompatibility of a long-range exchange interaction mediated by effective-mass-like states and of robust local magnetic moment formation determined by strong on-site Hund's rule coupling. Before considering the experimental realisation of room-temperature ferromagnetic semiconductors by hole-doping MX_2 layers substitutionally, we use our computational results and analysis to review a number of recent computational studies based upon the same DFT plus supercell methodology we have also used.

A. Other computational work

DFT is considered to be a suitable framework to use to study itinerant magnetism, both formally and in terms of practical calculations. It correctly predicts Fe, Co, and Ni to be the only transition metals that are ferromagnetic [11–13] and has been used to study a wide range of properties of very diverse magnetic materials [85,86]. The detailed results of practical DFT calculations depend on which of a large number of exchange-correlation functionals is used. Otherwise, different implementations of DFT can be used to reproducibly determine total energies and derived quantities if sufficient care is taken [87]. Before comparing our results to those of other computational studies, it will be useful to review a number of factors that need to be considered when carrying out DFT calculations as well as a number of open issues.

All of the computational studies of doped MX_2 systems of which we are aware were performed by modeling substitutional dopants in $L\times M\times N$ repeated supercells of the type discussed in Sec. II with L chosen to be unity to model a TMD monolayer and with a large thickness of vacuum inserted to minimize the interaction of the monolayer with its periodic image in the c direction, perpendicular to the plane of the TMD monolayer. In the plane of the monolayer, the size of the $M\times N$ lateral supercell determines the lowest concentration of dopant that can be modelled. By looking at a single substitutional donor or acceptor dopant in an $N\times N$ supercell as a function of N [8], we can examine how closely we can approach the single-impurity limit described by the effective mass theory (EMT) referred to in Sec. III B 2. We already discussed in Sec. II how the near-universal choice of a GGA exchange-correlation functional leads to problems with the separation $\Delta_{K\Gamma} = \varepsilon_\upsilon(K) - \varepsilon_\upsilon(\Gamma)$ of the valence band maxima at the Γ and K/K' points of high symmetry compared to experiment and how this led us to instead use the L(S)DA approximation that describes $\Delta_{K\Gamma}$ much better.

The single-impurity limit is important because (i) it is desirable to achieve room-temperature ferromagnetic ordering with as low a dopant concentration as possible in order to retain the semiconducting properties of the MX_2 host and (ii) single impurities can be studied experimentally to verify the calculations in a well-defined limit [57,62]. As discussed at length for MoS_2:V(Nb and Ta) in [8], many of the different results found in the literature can be understood in terms of the choice of exchange-correlation potential or some technical aspect of the calculations such as plane-wave cutoff, k-point sampling, vacuum thickness, etc. We will not repeat this discussion here but instead consider two open issues that were not addressed in detail in [8].

1. Self-interaction, LDA+U

The first concerns how a single unpaired spin is treated in DFT. Consider the electronic structure of the JT-distorted $MoTe_2$:V impurity shown in Fig. 6(c). In the absence of spin polarization, the Fermi level is seen to lie in the spin-degenerate d_{xy} state corresponding to half a spin-up hole and half a spin-down hole. This unphysical feature (of fractions of indivisible particles) of DFT-LDA can be resolved by using spin-polarized DFT (SDFT) and a spin version of the LDA (LSDA) based upon the spin-polarized electron gas [9,10].

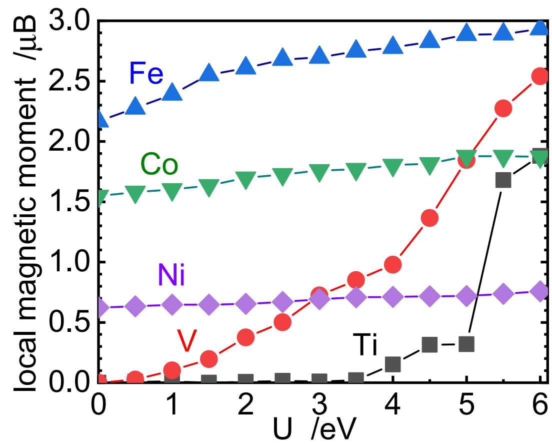

FIG. 13. Local magnetic moment per atom in μ_B as a function of Coulomb U (eV) on the 3d orbitals for hcp Ti, bcc V, bcc Fe, hcp Co, fcc Ni.

In the DFT for the total energy of a hydrogen atom [88], the Coulomb interaction of the single electron with itself (self-interaction) should be exactly canceled by the exchange-correlation energy term, as it is in orbital-based Hartree-Fock. In the LDA the cancellation is very incomplete, leading to a total energy of about −0.9 Rydberg. The LSDA introduces a Hund's-rule-like interaction of the electron density leading to an electron with a single spin (up or down) and a total energy of about −0.97 Rydberg, much closer to the correct result.

For many materials with partly filled and quite localized d or f shells, the LSDA "Hund's rule" solution was found to describe spectroscopic properties like the bandgap quite inadequately and attention focused on the atomic description of these states in terms of Coulomb integrals like the Hubbard U parameter [89–91] leading to an improved, mean-field description of the spectroscopic properties of such "correlated" materials termed L(S)DA+U [67]. A major disadvantage of the LDA+U approach is that it is not known what value of U should be used and it is usually chosen to reproduce some experimentally known quantity like the bandgap whereby the predictive capacity of DFT is lost. For example, we show in Fig. 13 the value of the magnetic moment "predicted" by LSDA+U as a function of the parameter U (actually $U - J$ in [67]) for a number of 3d transition metals where we have used the experimental lattice constants and crystal structures. For bcc Fe, hcp Co, and fcc Ni, the spin moment is overestimated for values of $U \sim 3-5$ eV typically used while hcp Ti and bcc V are incorrectly predicted to be ferromagnetic.

For single electron systems like the H atom, or single hole systems [92] like the single acceptors considered in this paper, there is no physical interaction of the electron or hole with itself, no question of the MX_2:V system being "strongly correlated". A justification for including a finite U on the V impurity might be that it mimics a self-interaction correction. However, this is not the justification given in the literature.

2. SP+SOC versus SOC+SP

The second open issue we consider relates to the simultaneous inclusion of spin-polarization (SP) and spin-orbit coupling (SOC) or the order in which they should be treated if included as perturbations. To predict an ordering temperature T_C, we (i) calculated the SIA in Sec. III B 7 by determining a spin-polarized solution of the Kohn-Sham equations and then included SOC as a perturbation ("force theorem") and (ii) estimated the interatomic exchange interaction $J(R)$ in Sec. IV by calculating the total energy of a pair of dopant atoms separated a distance R with the on-site spins aligned (FM) and antialigned (AFM), without SOC; by interpreting the energy difference $E_{FM} - E_{AFM}$ in terms of a Heisenberg model, we arrived at $J(R)$. Because of the large Bohr radius of the MX_2:V single acceptor e' states (Table VI), most of the corresponding hole is not on the V site and the SOC for these states is largely determined by that of the host. For the MoS_2 host considered in [8], the dominant exchange splitting of the a_1' state was comparable in magnitude to the spin-orbit splitting of the e' level and we did not attempt to include SOC in iterating the total energy to determine E_{FM} and E_{AFM}. For compounds containing W and Se or Te, this argument is less likely to be valid; spin polarization should ideally be included as a perturbation on top of SOC. The problem is that the spin dependence of the spin-dependent LSDA exchange-correlation potential depends (sensitively) on the spin density and can only be determined by an iterative self-consistent field (SCF) procedure. Including SOC doubles the size of the Hamiltonian that must be diagonalized and becomes roughly eight times more expensive; a factor of two is regained because spin-up and spin-down no longer need to be treated separately. The resulting factor of four is probably an underestimate of the true computational cost because the small size of the magnetic moments and exchange splitting makes many SCF iterations necessary. Including a finite value of U in this procedure makes the magnetism more robust and we will examine the result of doing so below.

3. Dopant-induced magnetic moments

Inducing magnetism in MX_2 monolayers by doping them p type with group IV and V transition metals (rather than with magnetic elements like Mn, Fe, Co, and Ni) has attracted a considerable amount of attention over the past decade. However, depending on the computational details, magnetic moments ranging from 0 [26,93] to 2.4 μ_B [94] are reported for single acceptors [22,95–102]; and from 0 [93,97,102,103] to 1.6 μ_B [94] for double acceptors. Because the width of the impurity band depends on the size of supercell used in a DFT calculation, we expect the magnetic moment to decrease as the supercell size is reduced causing the impurity bands to broaden [8]. We attribute the finding of single acceptors with magnetic moments per impurity of 0 μ_B [93,101] or less than 1 μ_B [98,99] to the use of small supercells. Calculated magnetic moments show a strong dependence on the inclusion of a Hubbard $U \sim$ 3–6 eV on the d orbitals of the dopant. This increases the splitting of the spin-up and spin-down dopant levels resulting in magnetic moments as large as 1.7 μ_B for single acceptors [94,97,99,100,102]. In the context of our remarks in Sec. V A 1, we note that a nonmagnetic system can be forced to become spin-polarized if U is larger than the separation of occupied and unoccupied levels. For example, with $U = 0$, MoS_2:Ti was reported to be nonmagnetic [94] but to become magnetic with an atomic moment of 1.6 μ_B with $U = 5.5$ eV. This large value of U causes the a_1' state of MoS_2:Ti (see Fig. 3) to split so that the hole is transferred to the e' state yielding a magnetic moment of well over 1 μ_B [94]. However, even with $U = 4-6$ eV, Tiwari did not find magnetism for Ti-doped MoS_2; presumably because of some other computational choice such as an inadequate supercell size [102].

The spatial distribution of the magnetization is strongly affected by the inclusion of a Hubbard U. This is illustrated in Fig. 14 for WSe_2:V where we find a total magnetic moment of 1.0 μ_B both in the LSDA and in the LSDA+U with $U = 3$ eV. It is only slightly reduced to 0.95 μ_B when SOC is included simultaneously with a $U = 3$ eV. However, where the moment on the V impurity is only 0.16 μ_B in the LSDA, including a Hubbard $U = 3$ eV leads to a much larger V moment of 1.47 μ_B (1.40 μ_B when SOC is included); this is compensated by antiparallel moments on the neighboring W and Se. This difference in spatial distribution is in principle amenable to experimental study using spin-polarized scanning tunneling microscopy [104]. We will see the consequences of this for the magnetic coupling between pairs of V dopants below.

Although the Hubbard U included in the calculations can account for the correlation effect of d electrons as on Mn [105], the choice of numerical value is notoriously fraught. For a (two-electron or) two-hole system, the Coulomb repulsion represented by a Hubbard U is more easily justified than for a (single electron or) hole especially when the Bohr radius is as large as we have found; in the single particle case the use of a Hubbard U might be justified in terms of self-interaction correction but that comes at the expense of predictive capability.

4. Comparison with the work of Duong et al.

Although many TMD host materials contain heavy elements for which the SOC is quite large, not much attention has been paid to the effect of this SOC in previous studies. An interesting exception is a computational study of WSe_2:V by Duong *et al.* [100] who found that including SOC led to an increase of the spatial extent of the magnetization of a single substitutional V impurity and proposed this as an explanation for observations of long range ferromagnetic ordering in doped MX_2 systems at elevated temperatures [22–28]. Using VASP, we have repeated these calculations, iterating the calculations to selfconsistency including SOC with a Hubbard $U = 3$ eV on the V impurity. We confirm that simultaneous inclusion of SOC and spin polarization leads to an enhancement of the (small) magnetic moments on W atoms far from the dopant. However, we also find that this occurs at the expense of larger antiparallel magnetic moments on the nearest-neighbor W and Se atoms, compare Figs. 14(b) and 14(c).

To see the effect this has on the exchange coupling, we performed total energy calculations for parallel and antiparallel aligned V pairs at a number of separations (using a 9×9 supercell because of the computational expense when the calculations are iterated with SOC). The upper curve (black squares) in Fig. 15 shows this coupling energy when SOC is not included. Compared to the LSDA results presented in the previous section, we see a huge increase in the strength of

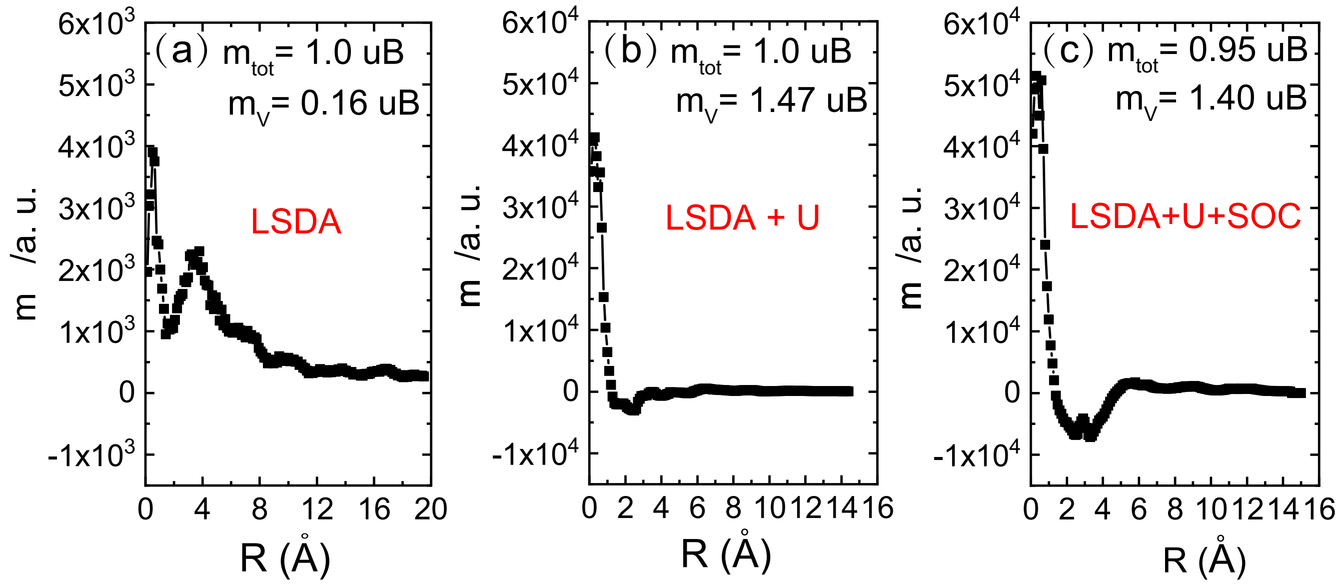

FIG. 14. Radial distribution of the magnetization arising from a single substitutional V acceptor in WSe_2 calculated for (a) the LSDA using a 12×12 supercell and using a 9×9 supercell (b) the LSDA+U with $U = 3$ eV, (c) the LSDA+U with $U = 3$ eV with SOC included in the SCF cycle.

the coupling energy, from a maximum value of ∼35 meV for V impurities on neighboring Mo sites (Fig. 11) to 225 meV (Fig. 15). This can be traced to the effect of U increasing the local magnetic moment of V from 0.16 μ_B to 1.47 μ_B, where the antiparallel magnetic moments on the W and Se neighbors limit the total magnetic moment to 1 μ_B. When SOC is included, the exchange interaction is reduced substantially,

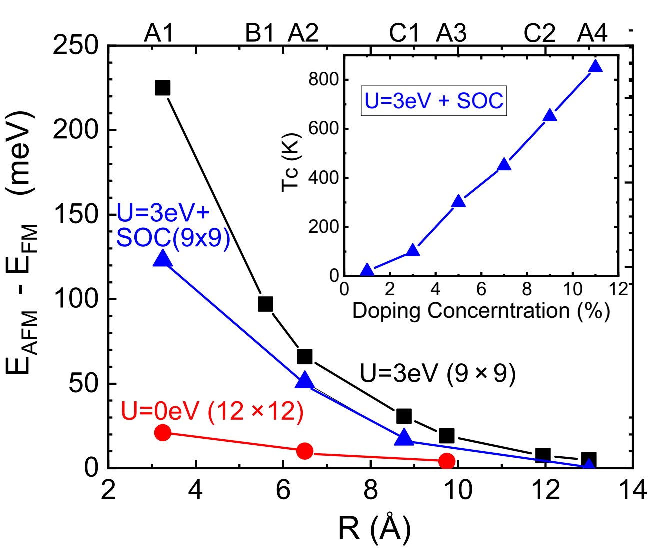

FIG. 15. Difference between the total energies of antiferromagnetic and ferromagnetic states for pairs of substitutional V impurities including relaxation in 9×9 supercells plotted as a function of their separation for WSe_2 monolayers when $U = 3$ eV is included on V. The LSDA results calculated in a 12×12 supercell are included for comparison ($U = 0$ eV). The solid lines are a guide to the eye. The labeling of the W sites surrounding the central impurity atom used on the top x axis is the same as that used in Fig. 3 of [8].

from 225 to 123 meV (blue triangles in Fig. 15) but remains much larger than the LSDA value; the results are dominated by the use of a Hubbard U. When the impurities are further apart (configuration A4 in Fig. 3 of [8]), SOC reduces the corresponding energy difference from 5.4 to −1.4 meV. This can be attributed to the SOC enhancement of the antiparallel magnetic moment on the W atoms closest to the V from −0.02 μ_B/W to −0.06 μ_B/W, which "screen" the exchange interaction between V pairs. The effect of U is to predict much higher critical temperature $T_C(x)$ for high dopant concentrations x; see the inset in Fig. 15.

Including a Hubbard U enhances the moment on the impurity site and leads to much larger exchange interactions. It also makes the iteration of the Kohn-Sham equations of DFT much more stable when SOC is included. The effect of SOC is large for WSe_2:V because of the large SOC of the 5d electrons of W. Tests for $MoSe_2$:V, indicate that the effect of SOC on the exchange interactions shown in Fig. 11 is much smaller so that our estimates of the ordering temperature should be a lower limit. While choosing intermediate values of U will lead to intermediate $T_C(x)$ curves, the basic underlying model of exchange coupling between effective mass like impurity states remains the same.

5. Comparison with the study of Tiwari et al.

In their calculations including SOC, Tiwari *et al.* have gone a step further than Duong *et al.* [100] by calculating the anisotropic interatomic exchange coupling $J_{ij}(R)$ and SIA with DFT calculations (including a Hubbard U in the range 4 to 6 eV) and combining these results in parameterized form with Monte Carlo simulations to estimate ordering temperatures for a large number of dopants in TMD monolayers [102]. Of relevance for the present discussion are their results for substitutional V and Ti in MoS_2, $MoSe_2$, $MoTe_2$, WS_2, and WSe_2. For all MX_2:Ti systems, they found

TABLE VIII. Single hole dopants in MX_2 TMDs for which room-temperature magnetic ordering has been reported.

$M+X$	S	Se	Te
Cr			
Mo	V [28]		V [26]; Ta [27]
W	V [22]	V [23,24,29]	

negligible magnetic moments, which agrees with our findings for the double-acceptor-doped diselenides and ditellurides when the JT distortion is included, Table III.

For MX_2:V, Tiwari *et al.* found FM ordering for the disulfides and diselenides but not for $MoTe_2$:V (which has a large magnetic moment of V up to 2 μ_B as listed in their Supplementary Table 3 but orders antiferromagnetically). For their most promising system, $MoSe_2$:V, Tiwari found $J(R)$ has a maximum value of ∼10 meV comparable to the value of ∼25 meV we report in Fig. 11(b) where $J(R)$ is half of the total energy difference between AFM and FM. However, they reported an ordering temperature of 224 K with a concentration of 15% V compared to our finding of ordering with this temperature for half of this concentration. We can trace the difference in this case to the choice of Hamiltonian used in the Monte Carlo simulations. For the doped systems, Tiwari *et al.* used a parameterized Heisenberg Hamiltonian that includes anisotropic exchange (less than 2%) and a single ion anisotropy of less than 1 meV ([102], Supplementary Material). The Heisenberg Hamiltonian allows the spin to rotate in three dimensions at finite temperature. In our paper, the large single ion anisotropy (as high as 10 meV per dopant) allows us to approximate the doped system with an Ising model. We attribute the difference in ordering temperatures to Tiwari's much smaller anisotropy. The differences in the single ion anisotropy can be understood in terms of the technical details of the two sets of calculations. Because he uses the GGA, we expect Tiwari's ordering of the a'_1 and e' defect states to be incorrect in the single-impurity limit because the GGA describes the relative positions of the Γ and K/K' VBM poorly compared to LDA. Using a Hubbard U to "account for the electron-electron interaction" of the single hole greatly enhances the exchange splitting of a'_1 and e' levels. We reproduced his calculations and found the holes reside mainly in the a'_1 levels that do not contribute to the magnetic anisotropy energy. Tiwari's calculation of an anisotropic interatomic exchange coupling $J_{ij}(R)$ based upon inclusion of SOC in the self-consistent SP iterations is in principle better than out treatment but comes at the price of limiting the size of supercell that he could use; 7×7 in his case versus our 12×12.

B. Experiments

Long-range defect- and impurity-induced magnetic ordering has been reported for the TMDs shown in Table VIII, with room-temperature ordering reported for the monovalent hole dopants, mostly vanadium, for dopant concentrations as low as 0.1% [23], 0.2% [26], or 0.4% [22]. Optimum concentrations have yet to be determined and the origin of the high-temperature ferromagnetism at these low doping concentrations is still an open question. Our calculations support the qualitative finding of ferromagnetism and provide a microscopic picture to interpret experiments but do not explain why the coupling is so strong at such low concentrations. It is conceivable that this is just a quantitative failing of the LDA; for the moment we focus on qualitative trends to suggest directions for further research.

The sensitivity of the magnetic properties of a monolayer of WSe_2:V to a back-gate bias has been invoked to argue for the relevance of an RKKY model [23]. In the RKKY model [85,86], localized atomic magnetic moments (transition metal d electrons; rare-earth f electrons) couple via the free electron gas between them (transition metal s electrons; rare-earth sd electrons). A gate voltage that can modulate the density of the electron gas changes the coupling between the localized magnetic moments. However, this is not the physical picture presented by our calculations nor indeed by those of Duong *et al.* [100]. Our DFT calculations show that there are no localized atomic moments nor is there a free-electron-like gas. In the single-impurity limit, there are single hole states bound to the valence band maxima with host M d character that are spread over many host M sites as well as the dopant atom. As the dopant concentration is increased, these single spins couple ferromagnetically and the impurity states form a narrow, partly filled, impurity band whose occupancy and the coupling between the spins, will be modified by gating. The manner in which it is changed should in principle be accessible to DFT calculations but this goes well beyond the scope of the present paper.

The occurrence of an optimum doping concentration of order 2% in WS_2:V by Zhang *et al.* [22] is indirect support for our finding that the ferromagnetic coupling between two vanadium impurity atoms in WS_2 is "quenched" below a critical separation [8], which we explained in terms of the preference for vanadium pairs to form singlet states in TM disulphides as a consequence of the near degeneracy of the impurity a'_1 and e' states when they are close. However, in TM diselenides and ditellurides, the a'_1 levels lie in the valence band and the quenching assumed by Pham *et al.* [24] for WSe_2:V is not supported by our LDA calculations.

In their calculations for WSe_2:V, Duong *et al.* [100] find a small magnetic moment on the W nearest-neighbor sites of the central impurity V that is antiparallel to the V moment as well as the moments on the remaining W hosts. We confirm this quantum mechanical description of the spatial distribution of a single hole state and note that it involves a single spin degree of freedom. Applying an external magnetic field or changing the temperature will certainly change this spatial distribution. However, the picture invoked by Pham *et al.* [24] to explain an observed *increase* of magnetization with temperature implies that the moments on the central impurity and on the neighboring W atoms are independent degrees of freedom and this explanation cannot be correct in detail.

In view of the key role that they play in the ferromagnetism of hole-doped MX_2 systems, it is important to verify the existence of the (a'_1 and) e' impurity states bound to the VBM that we have identified in all MX_2 systems studied, Fig. 3. One difficulty with finding these impurity levels is that experimental techniques like photoemission only detect occupied states; hole states can only be detected if they are occupied by, e.g., gating or by using inverse photoemission spectroscopy. Using scanning tunneling spectroscopy, Mallet observed bound impurity states at 140 meV above the VBM in a negatively charged V-doped WSe_2 monolayer whose Fermi level was determined by it having been grown on top of n-type epitaxial graphene [106]. Occupation of the hole state with an electron will quench the Coulomb binding of the V impurity and should substantially reduce the binding energy of about 60 meV that we find for WSe_2:V, Fig. 3. Instead, Mattel *et al.* interpret their data in terms of a V-related hole state with a binding energy of 140 meV. More detailed modeling and more extensive experiments are needed to resolve this discrepancy. Mallet's finding of three bound impurity states in a V_2 dimer does seem to imply the existence of multivalley impurity states.

C. Outlook

In spite of the large effective Bohr radius (~9.4 Å) and SIA (~4.7 meV) that we find for single substitutional V impurities in WSe_2, our study of the exchange interaction between V impurities does not predict WSe_2:V monolayers to be the most favorable system for realizing room-temperature ferromagnetism. Instead, 1H-CrX_2:V, $MoSe_2$:V, and $MoTe_2$:V are all predicted to exhibit stronger ferromagnetism than WSe_2:V (in the absence of a Hubbard U), Fig. 11. Edwards and Katsnelson have argued in the context of CaB_6 that the effective interaction and Curie temperature predicted by the Stoner criterion will not be reduced by correlation effects or spin wave excitations [107]. In this sense, systems with shallow and narrow impurity bands are very favorable for realizing high Curie temperature ferromagnetic semiconductors. Our Monte Carlo simulations identify 1H-$CrTe_2$ and $MoSe_2$ as the most promising of the systems we have considered. In view of the experimental observation of room-temperature ordering in WSe_2:V [23,24], the outlook therefore appears very bright.

The failure for CrX_2 to adopt the semiconducting hexagonal phase presents a serious challenge [108], in particular for realizing our prediction for $CrTe_2$:V. Because DFT studies for MX_2 monolayers indicate that the H structure is more stable than the T structure [109] and because of the large Bohr radius we find for all V-doped systems, Table VI, it may be simpler to start with $MoSe_2$ and explore the properties of the $Cr_xMo_{1-x}(Te_ySe_{1-y})_2$ alloy system rather than trying to prepare V-doped $CrTe_2$ itself.

VI. SUMMARY AND CONCLUSIONS

In this paper, a detailed study of hole doping of MoS_2 monolayers with single acceptors [8] has been extended to MX_2 monolayers with M = Cr, Mo, W and X = S, Se, Te that are doped with single (V, Nb, Ta) and double (Ti, Zr, Hf) acceptor dopants with a view to realizing a room-temperature ferromagnetic semiconductor. We identified the three impurity bound states induced by the substitutional dopants of group IV and V transition metal in MX_2 monolayers and studied the competition between spin polarization and JT distortion that determines the defect ground state in the single-impurity limit. We included spin-orbit coupling in order to determine the magnetic anisotropy in this limit, the so-called single ion anisotropy. This is out-of-plane for the single acceptors but in-plane for the double acceptors, which are therefore not suitable candidates for realizing magnetic semiconductors. Of the single acceptors, the LSDA exchange splitting is most robust for V making it the candidate of choice to study the exchange interaction between two impurity atoms. Intrinsic defects may enhance the local magnetic moment in p-doped MX_2 monolayers [28,29] but will localize the holes and reduce the range of the interatomic exchange interaction.

To estimate ordering temperatures, we calculated the energy difference between parallel (ferromagnetic) and antiparallel (antiferromagnetic) aligned pairs of V moments as a function of their separations in larger supercells and extracted from this energy difference an interatomic exchange interaction $J(R)$. Singlet states formed by close V pairs in MoS_2:V and WS_2:V monolayers represent a quenching of the magnetic moment (other single acceptors are similar to V). To avoid this quenching, the holes should occupy degenerate e' levels as happens in single-acceptor-doped MSe$_2$ and MTe$_2$ monolayers; this also gives rise to large single ion anisotropies because of the large spin-orbit interaction at the K/K' valley of MX_2 monolayers from which the e' levels derive. Partial occupation of these degenerate levels leads to Jahn-Teller distortions that can significantly reduce the exchange interaction as happens for $MoTe_2$:V, Fig. 10. However, for WSe_2:V, $MoSe_2$:V, and CrX_2:V monolayers we find negligible JT distortions, which can be attributed to the e' levels being very extended as indicated by their effective Bohr radius. $J(R)$ is used in Monte Carlo calculations to estimate the ordering temperature as a function of the dopant concentration and leads us to identify 1H $CrTe_2$:V and $MoSe_2$:V as the most promising candidates to explore experimentally. The possibility of preparing $M_xM'_{1-x}(X_yX'_{1-y})_2$ alloys presents numerous possibilities to tailor material properties.

ACKNOWLEDGMENTS

This work was financially supported by the "Nederlandse Organisatie voor Wetenschappelijk Onderzoek" (NWO) through the research programme of the former "Stichting voor Fundamenteel Onderzoek der Materie," (NWO-I, formerly FOM) and through the use of supercomputer facilities of NWO "Exacte Wetenschappen" (Physical Sciences). Y.G. thanks Anhui Normal University start-up grant for financial support.

[1] H. Ohno, H. Munekata, T. Penney, S. von Molnár, and L. L. Chang, Magnetotransport properties of p-type (In,Mn)As diluted magnetic III-V semiconductors, Phys. Rev. Lett. **68**, 2664 (1992).

[2] H. Ohno, A. Shen, F. Matsukura, A. Oiwa, A. Endo, S. Katsumoto, and Y. Iye, (Ga,Mn)As: A new diluted magnetic semiconductor based on GaAs, Appl. Phys. Lett. **69**, 363 (1996).

[3] T. Dietl, H. Ohno, F. Matsukura, J. Cibert, and D. Ferrand, Zener model description of ferromagnetism in zinc-blende magnetic semiconductors, Science **287**, 1019 (2000).

[4] T. Dietl, A ten-year perspective on dilute magnetic semiconductors and oxides, Nat. Mater. **9**, 965 (2010).

[5] T. Dietl and H. Ohno, Dilute ferromagnetic semiconductors: Physics and spintronic structures, Rev. Mod. Phys. **86**, 187 (2014).

[6] T. Jungwirth, J. Sinova, J. Mašek, J. Kučera, and A. H. MacDonald, Theory of ferromagnetic (III,Mn)V semiconductors, Rev. Mod. Phys. **78**, 809 (2006).

[7] K. Sato, L. Bergqvist, J. Kudrnovský, P. H. Dederichs, O. Eriksson, I. Turek, B. Sanyal, G. Bouzerar, H. Katayama-Yoshida, V. A. Dinh, T. Fukushima, H. Kizaki, and R. Zeller, First-principles theory of dilute magnetic semiconductors, Rev. Mod. Phys. **82**, 1633 (2010).

[8] Y. Gao, N. Ganguli, and P. J. Kelly, Itinerant ferromagnetism in *p*-doped monolayers of MoS_2, Phys. Rev. B **99**, 220406(R) (2019); DFT study of itinerant ferromagnetism in *p*-doped monolayers of MoS_2, **100**, 235440 (2019).

[9] U. von Barth and L. Hedin, A local exchange-correlation potential for the spin-polarized case: I, J. Phys. C: Solid State Phys. **5**, 1629 (1972).

[10] O. Gunnarsson and B. I. Lundqvist, Exchange and correlation in atoms, molecules, and solids by the spin-density-functional formalism, Phys. Rev. B **13**, 4274 (1976).

[11] O. Gunnarsson, Band model for magnetism of transition metals in the spin-density-functional formalism, J. Phys. F: Met. Phys. **6**, 587 (1976).

[12] O. K. Andersen, J. Madsen, U. K. Poulsen, O. Jepsen, and J. Kollar, Magnetic ground-state properties of transition-metals, Physica B+C **86-88**, 249 (1977).

[13] J. F. Janak, Uniform susceptibilities of metallic elements, Phys. Rev. B **16**, 255 (1977).

[14] H. Peelaers and C. G. Van de Walle, Effects of strain on band structure and effective masses in MoS_2, Phys. Rev. B **86**, 241401(R) (2012).

[15] N. D. Mermin and H. Wagner, Absence of ferromagnetism or antiferromagnetism in one- or two-dimensional isotropic Heisenberg models, Phys. Rev. Lett. **17**, 1133 (1966).

[16] P. C. Hohenberg, Existence of long-range order in one and two dimensions, Phys. Rev. **158**, 383 (1967).

[17] S. A. Leonel, A. Oliveira, B. V. Costa, and P. Coura, Comparative study between a two-dimensional anisotropic Heisenberg antiferromagnet with easy-axis single-ion anisotropy and one with easy-axis exchange anisotropy, J. Magn. Magn. Mater. **305**, 157 (2006).

[18] L. Onsager, Crystal statistics. I. A two-dimensional model with an order-disorder transition, Phys. Rev. **65**, 117 (1944).

[19] C. N. Yang, The spontaneous magnetization of a two-dimensional Ising model, Phys. Rev. **85**, 808 (1952).

[20] K. Binder, Finite size scaling analysis of Ising model block distribution functions, Z. Phys. B **43**, 119 (1981).

[21] D. P. Landau and K. Binder, *A Guide to Monte Carlo Simulations in Statistical Physics*, 3rd ed. (Cambridge University Press, Cambridge, 2009).

[22] F. Zhang, B. Zheng, A. Sebastian, D. H. Olson, M. Liu, K. Fujisawa, Y. T. H. Pham, V. O. Jimenez, V. Kalappattil, L. Miao *et al.*, Monolayer vanadium-doped tungsten disulfide: A room-temperature dilute magnetic semiconductor, Adv. Sci. **7**, 2001174 (2020).

[23] S. Yun, D. Duong, M. Doan, K. Singh, T. Phan, W. Choi, Y. Kim, and Y. Lee, Ferromagnetic order at room temperature in monolayer WSe_2 semiconductor via vanadium dopant, Adv. Sci. **7**, 1903076 (2020).

[24] Y. T. H. Pham, M. Liu, V. O. Jimenez, Z. Yu, V. Kalappattil, F. Zhang, K. Wang, T. Williams, M. Terrones, and M.-H. Phan, Tunable ferromagnetism and thermally induced spin flip in vanadium-doped tungsten diselenide monolayers at room temperature, Adv. Mater. **32**, 2003607 (2020).

[25] Z. Guguchia, A. Kerelsky, D. Edelberg, S. Banerjee, F. von Rohr, D. Scullion, M. Augustin, M. Scully, D. A. Rhodes, Z. Shermadini *et al.*, Magnetism in semiconducting molybdenum dichalcogenides, Sci. Adv. **4**, eaat3672 (2018).

[26] P. M. Coelho, H. Komsa, K. Lasek, V. Kalappattil, J. Karthikeyan, M.-H. Phan, A. V. Krasheninnikov, and M. Batzill, Room-temperature ferromagnetism in $MoTe_2$ by post-growth incorporation of vanadium impurities, Advan. Elect. Mater. **5**, 1900044 (2019).

[27] L. Yang, H. Wu, W. Zhang, X. Lou, Z. Xie, X. Yu, Y. Liu, and H. Chang, Ta doping enhanced room-temperature ferromagnetism in 2D semiconducting $MoTe_2$ nanosheets, Adv. Electron. Mater. **5**, 1900552 (2019).

[28] W. Hu, H. Tan, H. Duan, G. Li, N. Li, Q. Ji, Y. Lu, Y. Wang, Z. Sun, F. Hu *et al.*, Synergetic effect of substitutional dopants and sulfur vacancy in modulating the ferromagnetism of MoS_2 nanosheets, ACS Appl. Mater. Interfaces **11**, 31155 (2019).

[29] S. J. Yun, B. W. Cho, T. Dinesh, D. H. Yang, Y. I. Kim, J. W. Jin, S.-H. Yang, T. D. Nguyen, Y.-M. Kim, K. K. Kim *et al.*, Escalating ferromagnetic order via Se-vacancies near vanadium in WSe_2 monolayers, Adv. Mater. **34**, 2106551 (2022).

[30] P. E. Blöchl, Projector augmented-wave method, Phys. Rev. B **50**, 17953 (1994).

[31] G. Kresse and J. Hafner, *Ab initio* molecular dynamics for open-shell transition metals, Phys. Rev. B **48**, 13115 (1993).

[32] G. Kresse and J. Furthmüller, Efficient iterative schemes for *ab initio* total-energy calculations using a plane-wave basis set, Phys. Rev. B **54**, 11169 (1996).

[33] G. Kresse and D. Joubert, From ultrasoft pseudopotentials to the projector augmented-wave method, Phys. Rev. B **59**, 1758 (1999).

[34] J. P. Perdew and A. Zunger, Self-interaction correction to density-functional approximations for many-electron systems, Phys. Rev. B **23**, 5048 (1981).

[35] M. Methfessel and A. T. Paxton, High-precision sampling for Brillouin-zone integration in metals, Phys. Rev. B **40**, 3616 (1989).

[36] O. Jepson and O. K. Andersen, Electronic structure of hcp ytterbium, Solid State Commun. **9**, 1763 (1971).

[37] P. E. Blöchl, O. Jepsen, and O. K. Andersen, Improved tetrahedron method for Brillouin-zone integrations, Phys. Rev. B **49**, 16223 (1994).

[38] K. D. Bronsema, J. L. D. Boer, and F. Jellinek, On the structure of molybdenum diselenide and disulfide, Z. Anorg. Allg. Chem **540**, 15 (1986).

[39] K. F. Mak, C. Lee, J. Hone, J. Shan, and T. F. Heinz, Atomically thin MoS_2: A new direct-gap semiconductor, Phys. Rev. Lett. **105**, 136805 (2010).

[40] W. C. Jin, P. C. Yeh, N. Zaki, D. T. Zhang, J. T. Sadowski, A. Al-Mahboob, A. M. van der Zande, D. A. Chenet, J. I. Dadap, I. P. Herman *et al.*, Direct measurement of the thickness-dependent electronic band structure of MoS_2 using angle-resolved photoemission spectroscopy, Phys. Rev. Lett. **111**, 106801 (2013).

[41] Y. Zhang, T. Chang, B. Zhou, Y. Cui, H. Yan, Z. Liu, F. Schmitt, J. Lee, R. Moore, Y. Chen *et al.*, Direct observation of the transition from indirect to direct bandgap in atomically thin epitaxial $MoSe_2$, Nat. Nanotechnol. **9**, 111 (2014).

[42] N. R. Wilson, P. V. Nguyen, K. Seyler, P. Rivera, A. J. Marsden, Z. P. L. Laker, G. C. Constantinescu, V. Kandyba, A. Barinov, N. D. M. Hine *et al.*, Determination of band offsets, hybridization, and exciton binding in 2D semiconductor heterostructures, Sci. Adv. **3**, e1601832 (2017).

[43] O. Knop and R. D. MacDonald, Chalcogenides of the transition elements: III. Molybdenum ditelluride, Can. J. Chem. **39**, 897 (1961).

[44] C. Ruppert, O. B. Aslan, and T. F. Heinz, Optical properties and band gap of single- and few-layer $MoTe_2$ crystals, Nano Lett. **14**, 6231 (2014).

[45] W. J. Schutte, J. L. de Boer, and F. Jellinek, Crystal structures of tungsten disulfide and diselenide, Can. J. Chem. **70**, 207 (1987).

[46] S. Tongay, W. Fan, J. Kang, J. Park, U. Koldemir, J. Suh, D. S. Narang, K. Liu, J. Ji, J. Li *et al.*, Tuning interlayer coupling in large-area heterostructures with CVD grown MoS_2 and WS_2 monolayers, Nano Lett. **14**, 3185 (2014).

[47] C. Kastl, C. T. Chen, R. J. Koch, B. Schuler, T. R. Kuykendall, A. Bostwick, C. Jozwiak, T. Seyller, E. Rotenberg, A. Weber-Bargioni *et al.*, Multimodal spectromicroscopy of monolayer WS_2 enabled by ultra-clean van der Waals epitaxy, 2D Mater. **5**, 045010 (2018).

[48] W.-T. Hsu, L.-S. Lu, D. Wang, J.-K. Huang, M.-Y. Li, T.-R. Chang, Y.-C. Chou, Z.-Y. Juang, H.-T. Jeng, L.-J. Li, and W.-H. Chang, Evidence of indirect gap in monolayer WSe_2, Nat. Commun. **8**, 929 (2017).

[49] S. Manzeli, D. Ovchinnikov, D. Pasquier, O. V. Yazyev, and A. Kis, 2D transition metal dichalcogenides, Nat. Rev. Mater. **2**, 17033 (2017).

[50] C. F. van Bruggen, R. J. Haange, G. A. Wiegers, and D. K. G. de Boer, $CrSe_2$, a new layered dichalcogenide, Physica B+C **99**, 166 (1980).

[51] C. M. Fang, C. F. van Bruggen, R. A. de Groot, G. A. Wiegers, and C. Haas, The electronic structure of the metastable layer compound 1T-$CrSe_2$, J. Phys.: Condens. Matter **9**, 10173 (1997).

[52] M. R. Habib, S. Wang, W. Wang, H. Xiao, S. M. Obaidulla, A. Gayen, Y. Khan, H. Chen, and M. Xu, Electronic properties of polymorphic two-dimensional layered chromium disulphide, Nanoscale **11**, 20123 (2019).

[53] J. A. Wilson and A. D. Yoffe, Transition metal dichalcogenides discussion and interpretation of observed optical, electrical and structural properties, Adv. Phys. **18**, 193 (1969).

[54] N. Onofrio, D. Guzman, and A. Strachan, Novel doping alternatives for single-layer transition metal dichalcogenides, J. Appl. Phys. **122**, 185102 (2017).

[55] J. Karthikeyan, H. P. Komsa, M. Batzill, and A. V. Krasheninnikov, Which transition metal atoms can be embedded into two-dimensional molybdenum dichalcogenides and add magnetism? Nano Lett. **19**, 4581 (2019).

[56] S. T. Pantelides, The electronic structure of impurities and other point defects in semiconductors, Rev. Mod. Phys. **50**, 797 (1978).

[57] M. Lannoo and J. Bourgoin, in *Point Defects in Semiconductors I: Theoretical Aspects*, edited by M. Cardona, P. Fulde, and H.-J. Queisser, Springer Series in Solid-State Sciences Vol. 22 (Springer, Berlin, 1981).

[58] M. Altarelli and F. Bassani, Impurity states: Theoretical, in *Handbook on Semiconductors edited by T. S. Moss*, edited by W. Paul (North-Holland, Amsterdam, 1982), Vol. 1, pp. 269–322.

[59] Even if the impurity bandwidth is much smaller than the exchange splitting, incompletely filled states can be degenerate at the Fermi level with noninteger occupation numbers [110,111].

[60] H. A. Jahn and E. Teller, Stability of polyatomic molecules in degenerate electronic states. I. Orbital degeneracy, Proc. Roy. Soc. A **161**, 220 (1937).

[61] T. Inui, Y. Tanabe, and Y. Onodera, in *Group Theory and its Applications in Physics*, 2nd ed., edited by M. Carona, P. Fulde, K. von Klitzing, and H.-J. Queisser, Springer Series in Solid-State Sciences Vol. 78 (Springer, Berlin, 1996).

[62] J. Bourgoin and M. Lannoo, in *Point Defects in Semiconductors II: Experimental Aspects*, edited by M. Cardona, P. Fulde, and H.-J. Queisser, Springer Series in Solid-State Sciences Vol. 35 (Springer, Berlin, 1983).

[63] In the simplest case, x is the symmetry-lowering displacement of a single atom. More generally, it represents a "collective coordinate" describing some more complex distortion of the central and surrounding atoms.

[64] A single electron or hole does not experience a net exchange interaction. However, in the extension of density functional theory to spin, the introduction of a spin-dependent exchange-correlation potential [9,10] leads to an exchange splitting of the Kohn-Sham eigenvalues even for a hydrogen atom [88] and a lowering of the total ground state energy. The scheme shown in [4] represents these Kohn-Sham eigenvalues.

[65] Z. Tariq, S. U. Rehman, X. Zhang, F. K. Butt, S. Feng, B. U. Haq, J. Zheng, B. Cheng, and C. Li, Pristine and Janus monolayers of vanadium dichalcogenides: Potential materials for overall water splitting and solar energy conversion, J. Mater. Sci. **56**, 12270 (2021).

[66] K. H. Michel, D. Cakir, C. Sevik, and F. M. Peeters, Piezoelectricity in two-dimensional materials: Comparative study between lattice dynamics and *ab initio* calculations, Phys. Rev. B **95**, 125415 (2017).

[67] S. L. Dudarev, G. A. Botton, S. Y. Savrasov, C. J. Humphreys, and A. P. Sutton, Electron-energy-loss spectra and the structural stability of nickel oxide: An LSDA+U study, Phys. Rev. B **57**, 1505 (1998).

[68] B. Huang, G. Clark, E. Navarro-Moratalla, D. R. Klein, R. Cheng, K. L. Seyler, D. Zhong, E. Schmidgall, M. A. McGuire, D. H. Cobden *et al.*, Layer-dependent ferromagnetism in a van der Waals crystal down to the monolayer limit, Nature (London) **546**, 270 (2017).

[69] Z. Fei, B. Huang, P. Malinowski, W. Wang, T. Song, J. Sanchez, W. Yao, D. Xiao, X. Zhu, A. F. May *et al.*,

Two-dimensional itinerant ferromagnetism in atomically thin Fe_3GeTe_2, Nat. Mater. **17**, 778 (2018).
[70] Y. Deng, Y. Yu, Y. Song, J. Zhang, N. Z. Wang, Z. Sun, Y. Yi, Y. Z. Wu, S. Wu, J. Zhu *et al.*, Gate-tunable room-temperature ferromagnetism in two-dimensional Fe_3GeTe_2, Nature (London) **563**, 94 (2018).
[71] C. Xu, J. Feng, H. Xiang, and L. Bellaiche, Interplay between Kitaev interaction and single ion anisotropy in ferromagnetic CrI_3 and $CrGeTe_3$ monolayers, npj Comput. Mater. **4**, 57 (2018).
[72] A. R. Mackintosh and O. K. Andersen, The electronic structure of transition metals, in *Electrons at the Fermi Surface*, edited by M. Springford (Cambridge University Press, Cambridge, 1980), pp. 149–224.
[73] V. Heine, Electronic structure from the point of view of the local atomic environment, in *Solid State Physics*, edited by H. Ehrenreich, F. Seitz, and D. Turnbull (Academic Press, New York, 1980), Vol. 35, pp. 1–123.
[74] W. Kohn and L. J. Sham, Self-consistent equations including exchange and correlation effects, Phys. Rev. **140**, A1133 (1965).
[75] G. H. O. Daalderop, P. J. Kelly, and M. F. H. Schuurmans, First-principles calculation of the magnetocrystalline anisotropy energy of iron, cobalt and nickel, Phys. Rev. B **41**, 11919 (1990); G. H. O. Daalderop, P. J. Kelly, and F. J. A. den Broeder, Prediction and confirmation of perpendicular magnetic anisotropy in Co/Ni multilayers, Phys. Rev. Lett. **68**, 682 (1992); G. H. O. Daalderop, P. J. Kelly, and M. F. H. Schuurmans, Magnetic anisotropy of a free-standing Co monolayer and of multilayers which contain Co monolayers, Phys. Rev. B **50**, 9989 (1994).
[76] J. Hong, Z. Hu, M. Probert, K. Li, D. Lv, X. Yang, L. Gu, N. Mao, Q. Feng, L. Xie *et al.*, Exploring atomic defects in molybdenum disulphide monolayers, Nat. Commun. **6**, 6293 (2015).
[77] S. Wang, A. Robertson, and J. H. Warner, Atomic structure of defects and dopants in 2D layered transition metal dichalcogenides, Chem. Soc. Rev. **47**, 6764 (2018).
[78] H. I. Rasool, C. Ophus, and A. Zettl, Atomic defects in two dimensional materials, Adv. Mater. **27**, 5771 (2015).
[79] H. P. Komsa and A. V. Krasheninnikov, Native defects in bulk and monolayer MoS_2 from first principles, Phys. Rev. B **91**, 125304 (2015).
[80] W.-F. Li, C. Fang, and M. A. van Huis, Strong spin-orbit splitting and magnetism of point defect states in monolayer WS_2, Phys. Rev. B **94**, 195425 (2016).
[81] S. Haldar, H. Vovusha, M. K. Yadav, O. Eriksson, and B. Sanyal, A systematic study of structural, electronic and optical properties of atomic scale defects in 2D transition metal dichalcogenides MX_2 (M = Mo, W; X = S, Se, Te), Phys. Rev. B **92**, 235408 (2015).
[82] S.-Z. Yang, W. Sun, Y.-Y. Zhang, Y. Gong, M. P. Oxley, A. R. Lupini, P. M. Ajayan, M. F. Chisholm, S. T. Pantelides, and W. Zhou, Direct cation exchange in monolayer MoS_2 via recombination-enhanced migration, Phys. Rev. Lett. **122**, 106101 (2019).
[83] I. Tanabe, M. Gomez, W. C. Coley, D. Le, E. M. Echeverria, G. Stecklein, V. Kandyba, S. K. Balijepalli, V. Klee, A. E. Nguyen *et al.*, Band structure characterization of WS_2 grown by chemical vapor deposition, Appl. Phys. Lett. **108**, 252103 (2016).
[84] P.-C. Yeh, W. Jin, N. Zaki, D. Zhang, J. T. Liou, J. T. Sadowski, A. Al-Mahboob, J. I. Dadap, I. P. Herman, P. Sutter, and R. M. Osgood, Jr., Layer-dependent electronic structure of an atomically heavy two-dimensional dichalcogenide, Phys. Rev. B **91**, 041407(R) (2015).
[85] J. Kübler, *Theory of Itinerant Electron Magnetism* (Oxford University Press, Oxford, 2000).
[86] P. Mohn, in *Magnetism in the Solid State: An Introduction*, edited by M. Cardona, P. Fulde, K. von Klitzing, and H.-J. Queisser, Springer Series in Solid-State Sciences Vol. 134 (Springer, Berlin, 2003).
[87] K. Lejaeghere, G. Bihlmayer, T. Björkman, P. Blaha, S. Blügel, V. Blum, D. Caliste, I. E. Castelli, S. J. Clark, A. D. Corso *et al.*, Reproducibility in density functional theory calculations of solids, Science **351**, aad3000 (2016).
[88] O. Gunnarsson, B. I. Lundqvist, and J. W. Wilkins, Contribution to the cohesive energy of simple metals: Spin-dependent effect, Phys. Rev. B **10**, 1319 (1974).
[89] V. I. Anisimov, J. Zaanen, and O. K. Andersen, Band theory and Mott insulators: Hubbard u instead of stoner i, Phys. Rev. B **44**, 943 (1991).
[90] I. V. Solovyev, P. H. Dederichs, and V. I. Anisimov, Corrected atomic limit in the local-density approximation and the electronic structure of d impurities in Rb, Phys. Rev. B **50**, 16861 (1994).
[91] A. I. Liechtenstein, V. I. Anisimov, and J. Zaanen, Density-functional theory and strong interactions: Orbital ordering in Mott-Hubbard insulators, Phys. Rev. B **52**, R5467(R) (1995).
[92] H. A. Bethe and R. Jackiw, *Intermediate Quantum Mechanics*, 3rd ed., edited by D. Pines (Benjamin Cummings, Menlo Park, CA, 1986).
[93] K. Dolui, I. Rungger, C. Das Pemmaraju, and S. Sanvito, Possible doping strategies for MoS_2 monolayers: An ab initio study, Phys. Rev. B **88**, 075420 (2013).
[94] A. N. Andriotis and M. Menon, Tunable magnetic properties of transition metal doped MoS_2, Phys. Rev. B **90**, 125304 (2014).
[95] Q. Yue, S. Chang, S. Qin, and J. Li, Functionalization of monolayer MoS_2 by substitutional doping: A first-principles study, Phys. Lett. A **377**, 1362 (2013).
[96] S.-C. Lu and J.-P. Leburton, Electronic structures of defects and magnetic impurities in MoS_2 monolayers, Nanoscale Res. Lett. **9**, 676 (2014).
[97] N. Singh and U. Schwingenschlögl, Extended moment formation in monolayer WS_2 doped with 3d transition-metals, ACS Appl. Mater. Interfaces **8**, 23886 (2016).
[98] H. Li, S. Liu, S. Huang, D. Yin, C. Li, and Z. Wang, Impurity-induced ferromagnetism and metallicity of WS_2 monolayer, Ceramics Intl. **42**, 2364 (2016).
[99] M. Wu, X. Yao, Y. Hao, H. Dong, Y. Cheng, H. Liu, F. Lu, W. Wang, K. Cho, and W.-H. Wang, Electronic structures, magnetic properties and band alignments of 3d transition metal atoms doped monolayer MoS_2, Phys. Lett. A **382**, 111 (2018).
[100] D. L. Duong, S. J. Yun, Y. Kim, S.-G. Kim, and Y. H. Lee, Long-range ferromagnetic ordering in vanadium-doped WSe_2 semiconductor, Appl. Phys. Lett. **115**, 242406 (2019).

[101] M. Pan, J. T. Mullen, and K. W. Kim, First-principles analysis of magnetically doped transition-metal dichalcogenides, J. Phys. D: Appl. Phys. **54**, 025002 (2021).

[102] S. Tiwari, M. L. Van de Put, B. Sorée, and W. G. Vandenberghe, Magnetic order and critical temperature of substitutionally doped transition metal dichalcogenide monolayers, npj 2D Mater. Appl. **5**, 54 (2021).

[103] X. Zhao, C. Xia, T. Wang, and X. Dai, Electronic and magnetic properties of X-doped (X = Ti, Zr, Hf) tungsten disulphide monolayer, J. Alloys Compd. **654**, 574 (2016).

[104] R. Wiesendanger, Spin mapping at the nanoscale and atomic scale, Rev. Mod. Phys. **81**, 1495 (2009).

[105] C. J. Gil, A. Pham, A. Yu, and S. Li, An *a*b initio study of transition metals doped with WSe_2 for long-range room temperature ferromagnetism in two-dimensional transition metal dichalcogenide, J. Phys.: Condens. Matter **26**, 306004 (2014).

[106] P. Mallet, F. Chiapello, H. Okuno, H. Boukari, M. Jamet, and J.-Y. Veuillen, Bound hole states associated to individual vanadium atoms incorporated into monolayer WSe_2, Phys. Rev. Lett. **125**, 036802 (2020).

[107] D. M. Edwards and M. I. Katsnelson, High-temperature ferromagnetism of sp electrons in narrow impurity bands: Application to CaB_6, J. Phys.: Condens. Matter **18**, 7209 (2006).

[108] J. Su, K. Liu, F. Wang, B. Jin, Y. Guo, G. Liu, H. Li, and T. Zhai, Van der Waals 2D transition metal tellurides, Adv. Mater. Interfaces **6**, 1900741 (2019).

[109] C. Ataca, H. Şahin, and S. Ciraci, Stable, single-layer MX_2 transition-metal oxides and dichalcogenides in a honeycomb-like structure, J. Phys. Chem. C **116**, 8983 (2012).

[110] J. F. Janak, Proof that $\partial e/\partial n_i = \epsilon_i$ in density-functional theory, Phys. Rev. B **18**, 7165 (1978).

[111] R. O. Jones and O. Gunnarsson, The density functional formalism, its applications and prospects, Rev. Mod. Phys. **61**, 689 (1989).